



1 On the quality of RS41 radiosonde descent data

2 Bruce Ingleby¹, Martin Motl², Graeme Marlton³, David Edwards³, Michael Sommer⁴, Christoph von
3 Rohden⁴, Holger Vömel⁵, Hannu Jauhiainen⁶

4 ¹European Centre for Medium-Range Weather Forecasts, Reading, RG2 9AX, UK

5 ²Czech Hydrometeorological Institute, Prague, 14306, Czechia

6 ³Met Office, Exeter EX1 3PB, UK

7 ⁴Deutscher Wetterdienst (DWD)/GCOS Reference Upper Air Network (GRUAN) Lead Center, Lindenberg, Germany

8 ⁵National Center for Atmospheric Research, Boulder CO, 80301, USA

9 ⁶Vaisala Oyj, 01670 Vantaa, Finland

10
11 *Correspondence to:* Bruce Ingleby (bruce.ingleby@ecmwf.int)

12 **Abstract.** Radiosonde descent profiles have been available from tens of stations for several years now - mainly from Vaisala
13 RS41 radiosondes. They have been compared with the ascent profiles, with ECMWF short-range forecasts and with co-located
14 radio-occultation retrievals. Over this time our understanding of the data has grown, and the comparison also shed some light
15 on radiosonde ascent data. It has become clear that the fall rate is very variable and that it is an important factor, with high
16 fall rates being associated with temperature biases, especially at higher altitudes. Ascent winds are affected by pendulum
17 motion, on average descent winds are less affected by pendulum motion and are smoother. It is plausible that the true wind
18 variability in the vertical lies between that shown by ascent and descent profiles. The discrepancy indicates the need for
19 reference wind measurements.

20 1 Introduction

21 Radiosondes were first developed in the 1930s and have been used to measure profiles of temperature, humidity and wind
22 since then. There are now approximately 800 operational radiosonde stations worldwide, mostly providing ascents once or
23 twice per day. These are used for Numerical Weather Prediction (NWP), climate studies and other applications. The Global
24 Climate Observing System (GCOS) set up the GCOS Reference Upper-Air Network (GRUAN) to produce reference quality
25 data, with uncertainty estimates, from a subset of stations (Bodeker et al, 2016). Climate users, like GRUAN, tend to focus
26 on temperature and humidity. For NWP the winds are arguably more important (shown for aircraft data by Ingleby et al, 2021)
27 - partly because satellites provide more temperature and humidity information than wind information. One attraction of
28 radiosonde descent data is that there is very little additional cost involved and potentially an extra vertical profile, assuming
29 that the quality is acceptable. Whilst performing this study, it has become apparent that descent data prompts a re-examination
30 of ascent data and this can either support or challenge our views of the ascent data.

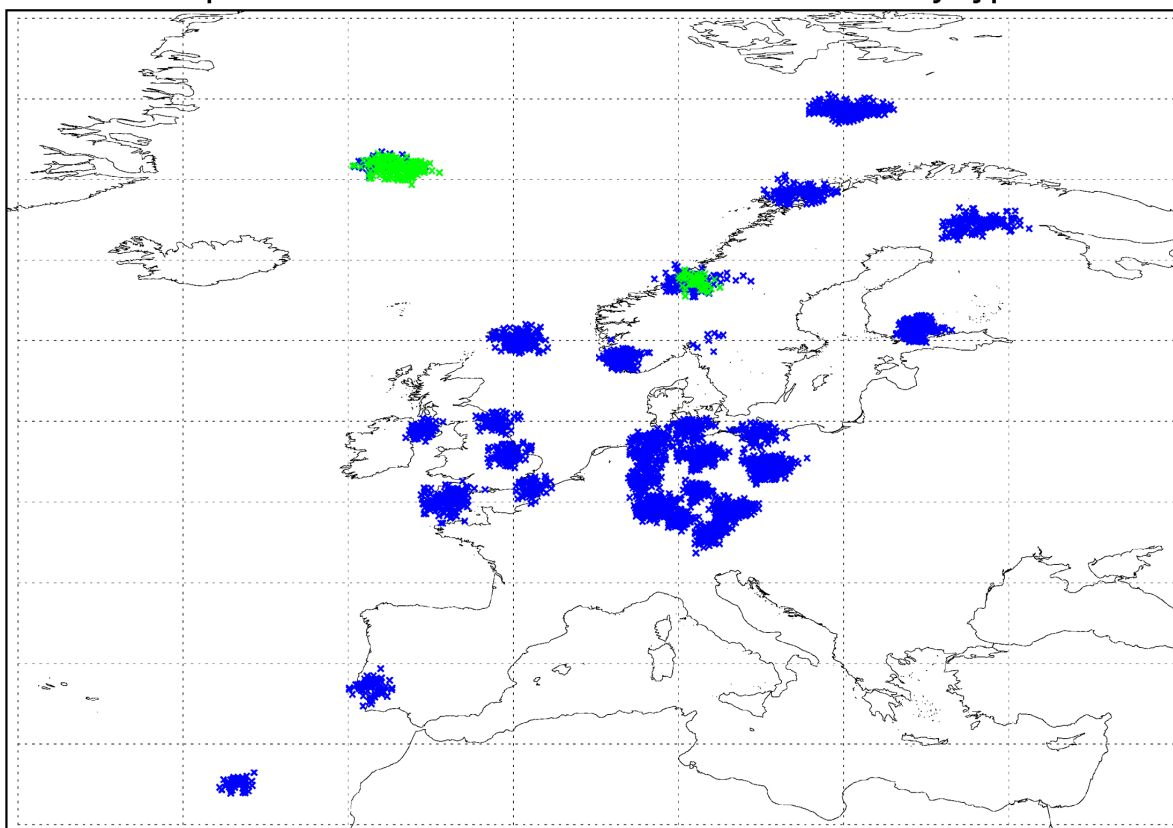


31 As radiosondes are designed to measure during the ascent, it is useful to consider how they differ from dropsondes which
32 always measure on descent. Dropsondes are launched from aircraft and are mainly used for sampling around tropical cyclones
33 and for field experiments. Radiosondes typically have the temperature and humidity sensors mounted diagonally above the
34 radiosonde body whereas dropsondes (e.g. Hock and Franklin, 1999) have the sensors underneath - in each case to sample air
35 undisturbed by the radiosonde body. The AVAPS (Advanced Vertical Atmospheric Profiling System) processing system used
36 by many dropsondes includes an ‘inertial’ correction for the delayed response to horizontal wind shear (Appendix of Hock
37 and Franklin, 1999). Modern radiosondes are usually on a line 30-55 m below the balloon whereas dropsondes are only 1 m
38 or less below a parachute. As noted by Wang et al (2008) ‘The dropsonde fall rate is much smoother than the radiosonde
39 ascent rate because of the radiosonde’s pendulum effect and self-induced balloon motion’. Typically dropsondes fall at about
40 10 m s^{-1} , just after launch it can be about 20 m s^{-1} before the parachute opens fully. As discussed below, radiosonde descent
41 can be much faster (to 100 m s^{-1} or more if no parachute is used) shortly after balloon burst. There has been some use of
42 controlled descent, by partial deflation of the balloon, for measurement of stratospheric humidity (Hurst et al, 2011). Zhang
43 et al (2019) tested the use of a low density ‘hard ball’ to give more consistent drag than a parachute when deriving the vertical
44 velocity of the air using a radiosonde descending from a height of about 10 km.

45
46 Figure 1 shows BUFR (Binary Universal Form for Representation of meteorological data) descent reports over Europe for
47 September-November 2019 (descent data were also available from New Zealand, not shown). BUFR allows the reporting of
48 high vertical resolution radiosonde data (Ingleby et al., 2016). Geller et al., (2021) found that in mid-2020 44% of operational
49 radiosonde stations were providing high vertical resolution ascent data. Since 2019 descent data has become available from
50 more European stations and a few in the Americas. After launch the balloon is advected horizontally by the wind, especially
51 at upper levels, and typically travels 50 to 300 km before burst with the larger distances being more common in winter (Seidel
52 et al., 2011).



Sep-Nov 2019: Descent data BUFR availability/type



53
 54 **Figure 1: Descent reports (burst positions) over Europe for September-November 2019, blue - Vaisala RS41, green - Modem M10.**
 55 **There were 14 stations from Germany, 6 each from UK and Norway and 2 each from Finland and Portugal.**

56 Figure 2 gives an indication of the number and vertical extent of descent profiles. Larger balloon size and fill volume is used
 57 to achieve higher altitudes. On average, radiosondes that achieve higher altitudes drift further horizontally, resulting in the
 58 radio signal to the launch station being lost at higher altitudes on descent due to obstruction by terrain or signal attenuation.
 59 This can be seen clearly in the UK results which have been split into automatic and manual launches: the manual launches use
 60 larger balloons and the number of descent reports starts to decline earlier, below 9 km. Automatic launchers are documented
 61 by Madonna et al. (2020). Some of the other countries use a mixture of manual and automatic launchers, but with little or no
 62 difference in balloon size. A small proportion of ascents do not have a corresponding descent report, often due to a fault
 63 developing with the radiosonde before or upon burst, leading to an automatic termination.

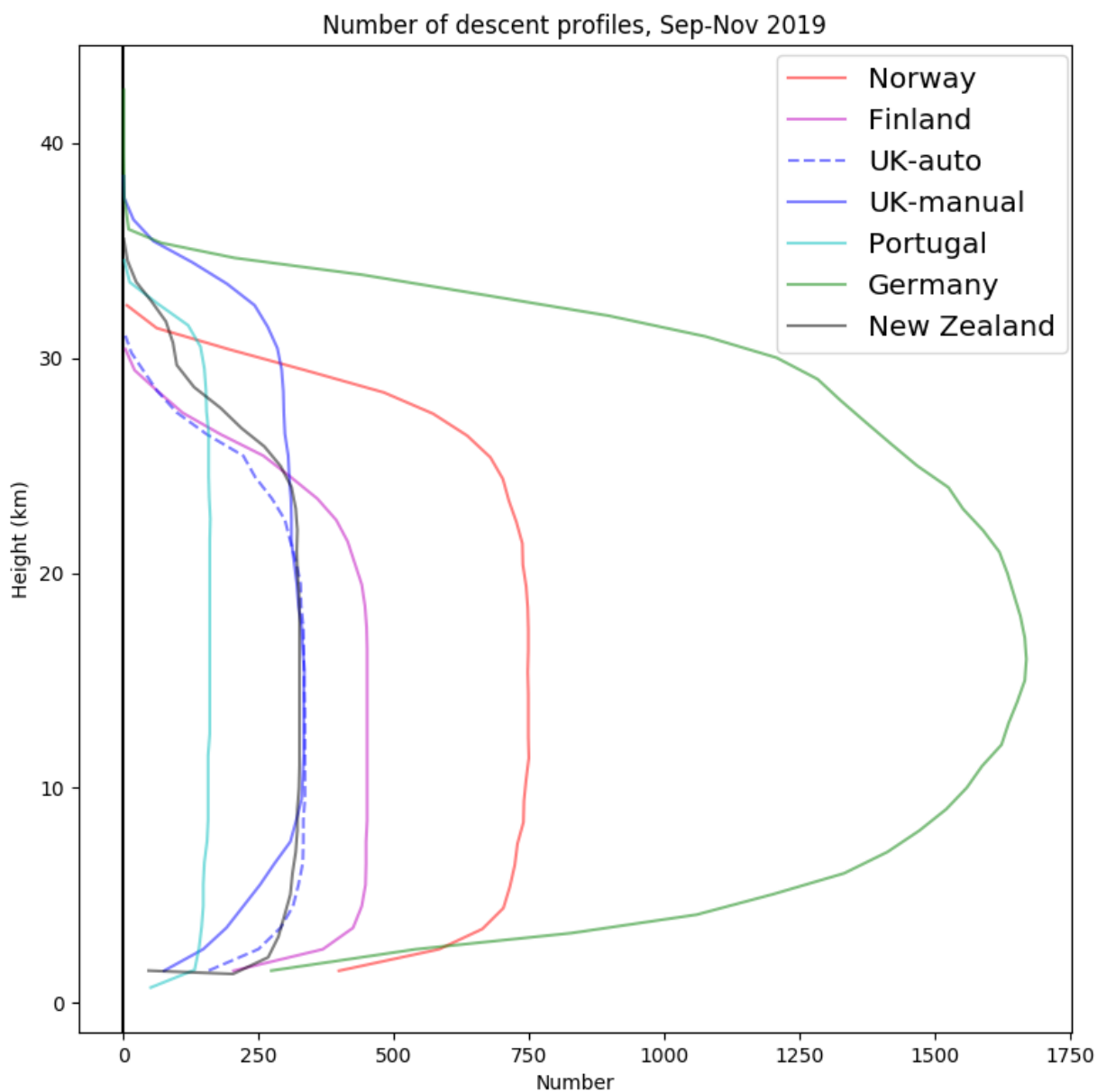
64 .

Country	Parachute	Pressure sensor	Balloon weight (g)
Norway	No	Yes	350 (01004*: 1500)
Finland	No	No	350
UK	Yes	No	350 (03005, 03808: 800+)



Germany	Yes	Yes	600 (also 300, 800) (10962: 1200+)
Portugal	Yes (2 stations)	Yes	600
New Zealand	No	No	350

65 Table 1. Summary of metadata for countries providing descent data in 2019. For balloon weight the most common value is
 66 given followed by others used in brackets, usually with an indication of the stations involved. (* station 01004 did not provide
 67 descent reports in 2019.)



68
 69 **Figure 2: Numbers of RS41 descent reports by height and country, September-November 2019.**



70

71 **2 Radiosonde ascent and descent**

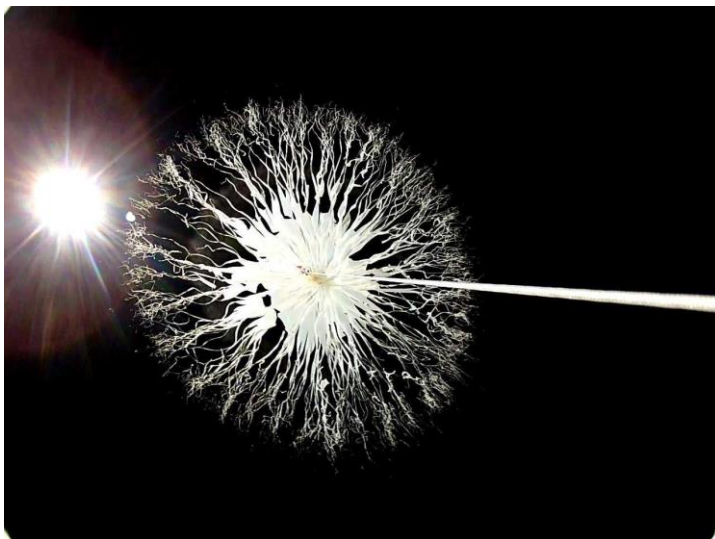
72 **2.1 What goes up must come down**

73 A balloon is filled with hydrogen or helium and ascends, attached by a string to the radiosonde (instrument package). Balloon
74 techniques are documented by WMO (2018b). The Vaisala RS41-SG radiosondes have a small sensor boom with temperature
75 and humidity sensors near the end, and wind and position are measured using a GPS receiver. Some models have a pressure
76 sensor, identified as the RS41-SGP (pressure is discussed in section 4.2). The measurements are transmitted back to the ground
77 station and processed there. Dirksen et al (2014) describe the GRUAN processing of the Vaisala RS92 and the instrument
78 accuracy; the operational BUFR reports come from the Vaisala processing. The Vaisala RS41 is the successor to the RS92
79 and is similar in many respects, but with improved humidity and temperature measurements (Edwards et al, 2014; Jensen et
80 al, 2016). As the balloon ascends it expands in diameter and eventually bursts causing the radiosonde to descend - transmission
81 of the measurements continues but traditionally processing stops at this point. When the radiosonde falls below the horizon
82 as seen from the ground station then it is no longer possible to receive the transmissions. Typically, the ascent takes 90-120
83 minutes (reaching altitudes of 30 or 35 km) and the descent takes 30 minutes or less. The upper part of the descent is close to
84 the upper part of the ascent in both time and space, usually with increasing separation as the radiosonde descends.

85 Some operators include a parachute, either inside or just below the balloon. The parachute slows the descent and is intended
86 to reduce the risk of damage to life and property when the radiosonde reaches the surface. In sparsely populated or island
87 countries a parachute may not be used.

88 From rare images of the balloon burst (figure 3) and recovered radiosondes (mainly those launched from Lindenberg, Germany
89 with extra instruments), shown in figure 4, and also from the motion on descent it is clear that a) sometimes the balloon bursts
90 completely or tears off at the nozzle and the parachute opens fully, b) sometimes the balloon tears open leaving strips attached,
91 these may get tangled with the parachute - which may partially 'free itself' later, c) sometimes the parachute ruptures and so
92 is ineffective. Where there is no parachute we speculate that sometimes the remains of the balloon act to slow the descent.
93 Note also that when complete, the mass of the balloon is typically several times that of the radiosonde (larger balloons are used
94 to reach higher altitudes, they are also sometimes used at night; the same balloon/amount of gas will reach higher in the daytime
95 on average). Some stations add extra instruments periodically, for example once a week Lerwick (03005) measures ozone as
96 well and a larger balloon and parachute are used.

97



98



99

100 Figure 3. Photographs of a bursting balloon (top) and parachute (orange) entangled in balloon remains (bottom). Balloon and
101 parachute were used for a frostpoint hygrometer launched at Lindenberg and are larger than those for a regular radiosonde
102 launch.

103



104

105 Figure 4. Collage of photographs showing balloon remnants (Totex TA and TX balloons of different size) and parachutes
106 (orange or silvery) after landing - Lindenberg launches.

107

108 On ascent the sensor boom projects above the radiosonde, so that it samples air that has not flowed over the body of the
109 radiosonde. On descent, with a working parachute, it should be in a similar position - so it may sample air that has flowed
110 over the radiosonde body, which has the potential to introduce biases or contamination. It is not known how a radiosonde
111 descending without a parachute is orientated, or if it may be tumbling.

112 2.2 Types of parachute and string length

113 For some manual launches a parachute (if used) is attached to the line not far below the balloon. Figure 4 shows that sometimes
114 the two can become entangled after balloon burst. For automated launches a parachute (if used) is stored within the balloon
115 and this seems to cause fewer entanglement problems. This can be used for manual launches too, and has been used at
116 Lindenberg for some years, but there is a small additional expense. In general, most of the parachutes are quite basic and do
117 not include a hole. Air can build up inside the parachute and suddenly spill out. It is clear from some of our results that
118 parachutes do not always open as intended.

119 In earlier decades the string connecting the balloon and the radiosonde may have been 10 m or less, but in the stratosphere the
120 balloon gets larger and there can be intermittent influences of the balloon wake upon the instruments (WMO, 1994; Luers and
121 Eskridge 1998; Söder et al 2019). For this reason longer suspensions are used now, WMO (2018a) suggests 40 m for



122 radiosondes ascending to 30 km or higher. In practice an ‘unwinder’ is used to increase the line length shortly after the
123 radiosonde launch (WMO, 2018b). The Vaisala unwinder for the RS41 gives 55 m when extended (Vaisala, 2017). We note
124 that while longer lines benefit stratospheric temperature measurements they cause larger amplitude pendulum motion in the
125 winds.

126 **2.3 Preparation of profile reports**

127 Data values are transmitted to the ground receiver every second and are processed by Vaisala MW41 software. Raw data
128 values, both ascent and descent, indexed by time are stored locally (the GRUAN archive makes the one second data available
129 for GRUAN sites). The MW41 software looks for a sustained decrease in altitude to determine the time of burst. In the past,
130 all later data would usually have been discarded but there is now an option to continue processing and to produce a separate
131 BUFR descent message using sequence 3 09 056 (WMO, 2019) designed for descent data. In 2019, as an interim measure, the
132 dropsonde sequence 3 09 053 was being used. As the timeliness of ascent data is critical for data users, it is preferable to
133 transmit the ascent profile as soon as possible after burst, followed by the descent data sent once the profile is completed.
134 BUFR from the European stations involved in this study is generally provided every two seconds (about 10 m separation in
135 the vertical during ascent).

136 The MW41 horizontal winds are derived primarily from Doppler processing of the Global Positioning System (GPS) signals
137 but the GPS locations are also used (GRUAN processing only uses the GPS positions). There is very good vertical resolution
138 but it also means that the winds sample the pendulum motion of the radiosonde - this is probably a mixture of planar and
139 conical pendulum motion. The period of the pendulum motion is a function of the length of line between the balloon or
140 parachute and the radiosonde. The processing attempts to filter out the pendulum motion (discussed briefly in Dirksen et al
141 2014), but the filtering is imperfect as discussed below.

142 **2.4 Descent fall rates**

143 The balloon and gas are chosen so that the ascent rate is about 5 m/s on average - however there is usually notable high
144 frequency variability probably due to pendulum motion. Especially in the stratosphere, there can be lower frequency signals
145 due to gravity waves and both of these features can be seen in Figure 5 (grey line, ascent). After the balloon bursts the
146 radiosonde falls very fast (over 70 m/s in this case) and then slows abruptly - presumably when the parachute opens fully.
147 After this there is a little high frequency variability (but much less than on the ascent) and a gradual decrease in descent rate
148 as the air density increases. Looking at a sample of Lindenberg descents over several weeks (supplementary material), some
149 exhibit an abrupt deceleration and others do not. Figure 6 shows descent rates from the station at Sola in Norway, without
150 parachutes. These do not show the abrupt deceleration, but do show a large range of descent rates. The slower descents tend
151 to have larger high frequency variability. We tentatively suggest that in these cases, the remains of the balloon are acting to
152 slow the descent and there is some pendulum motion. The variability in the descent rate may be due to variability in the mass



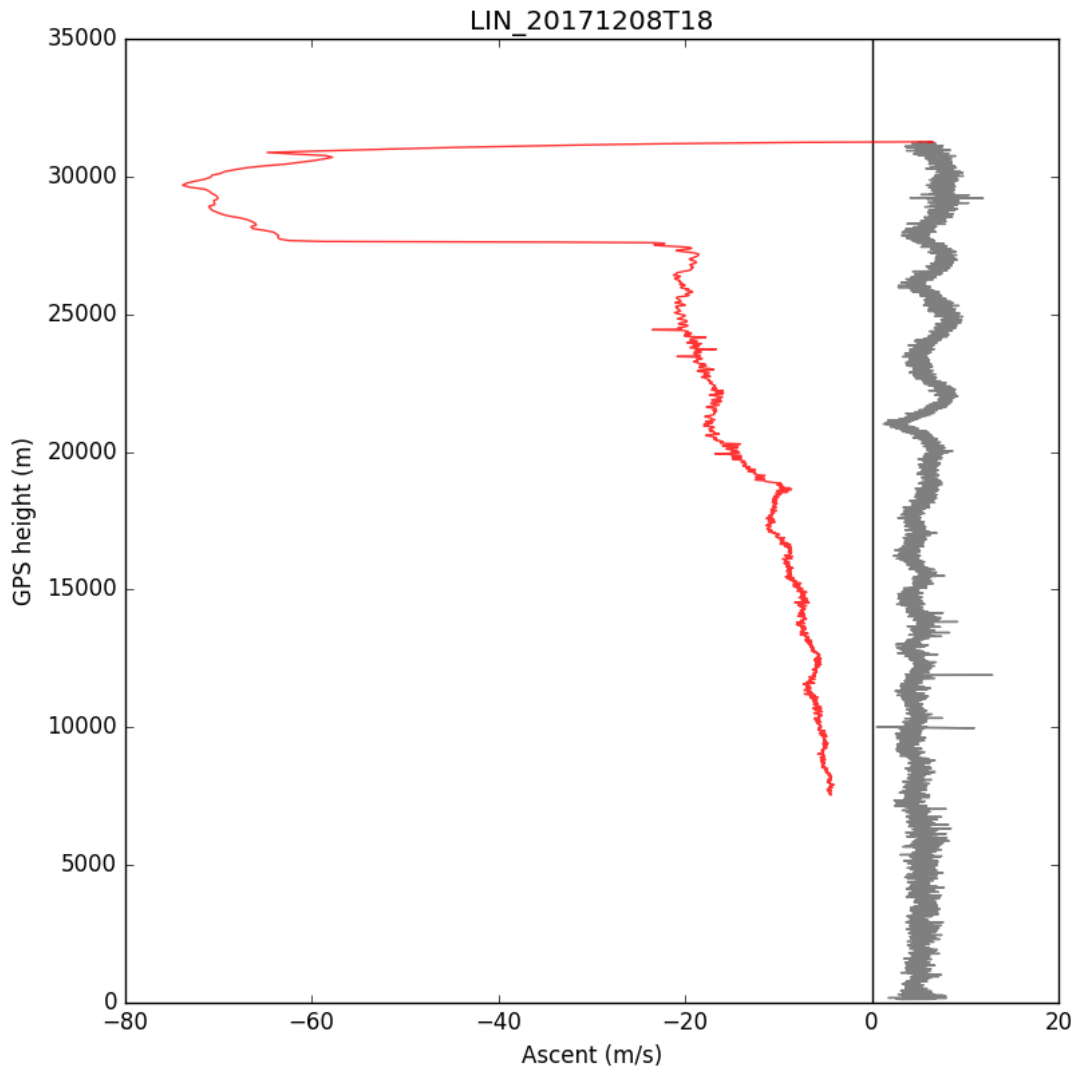
153 and shape of balloon remnants. Similar figures for several weeks of descents at Lindenberg are shown in the supplemental
154 material.

155 Mean descent rates by country are shown in Figure 7 (it should be remembered that this hides a lot of variability). For any
156 particular altitude those from Germany and the UK are slowest, reflecting their use of parachutes. Amongst the others there
157 is a large range. The Norwegian radiosondes fall faster than those from the other countries studied - it is unclear why they fall
158 faster than the Finnish radiosondes. In section 3 we focus on the four northern European countries (Norway, Finland, UK and
159 Germany) because they have similar upper air climatologies but different instrument characteristics. For Germany and Finland
160 the descent data received at ECMWF stopped on about 20 November 2019 linked to the move to the new BUFR template.
161 During 2020 the volume of descent profiles increased overall (e.g. France and Spain started sending them), although there was
162 also some disruption from the Covid pandemic.

163

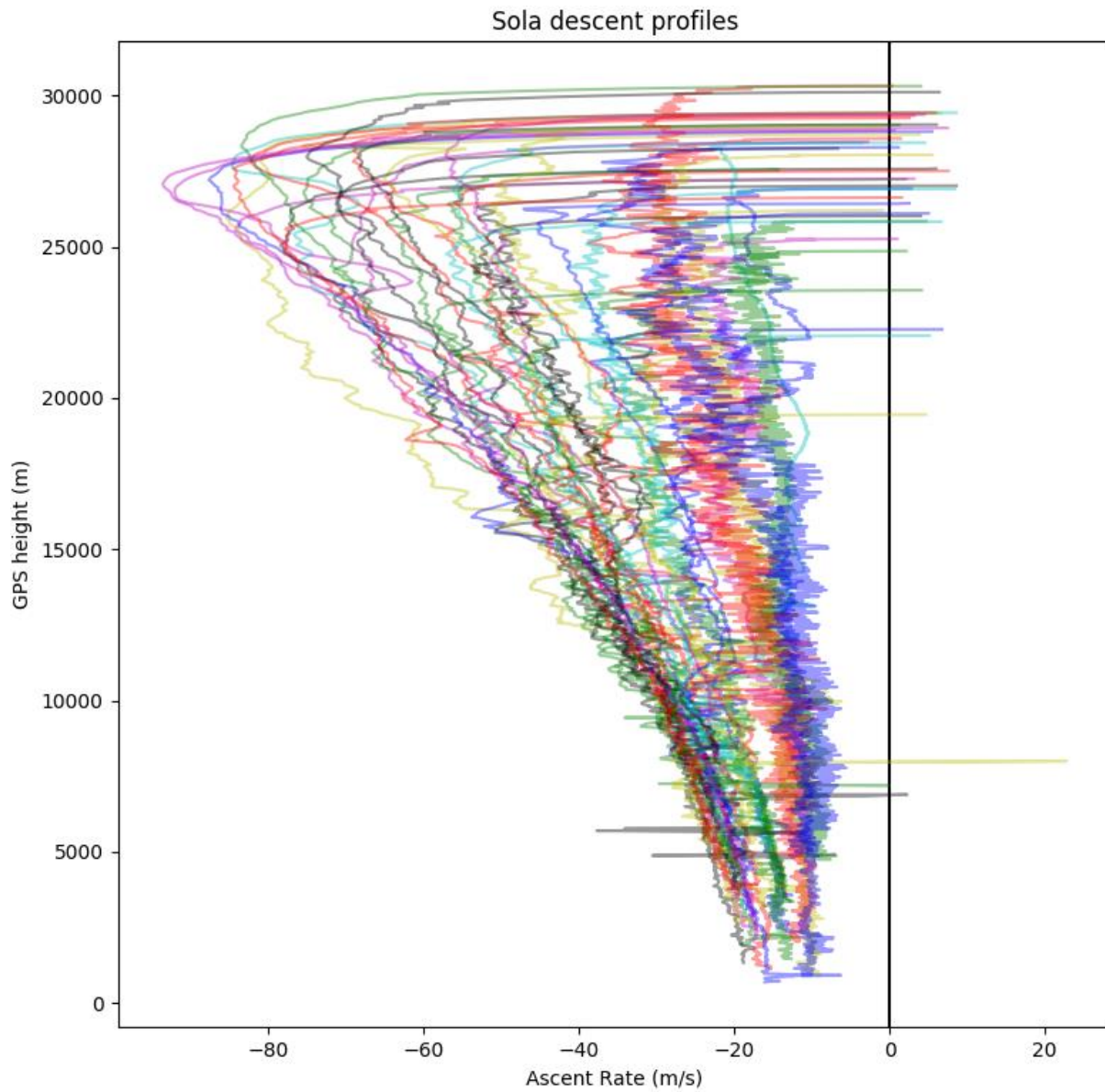
164

165



166

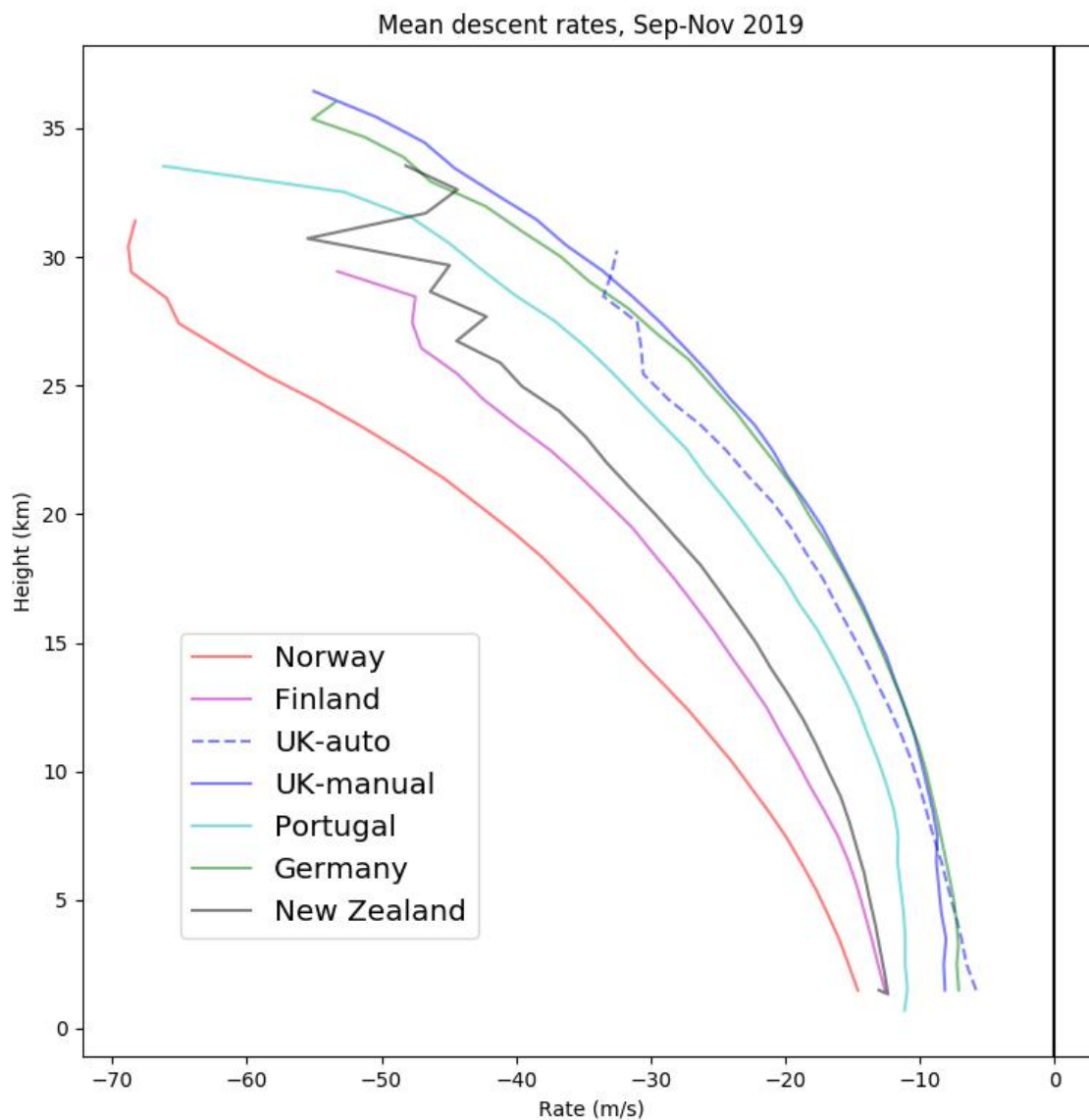
167 **Figure 5: Ascent (grey) and descent (red) speed - an example from Lindenberg (1 s data).**



168

169

Figure 6: Descent profiles from Sola (Norway, data courtesy of Terje Borge): 14 December 2019 - 5 January 2020.



170

171 **Figure 7: Mean descent rates for September-November 2019, same categories as Figure 2.**

172

173

174



175 2.5 Motion of radiosonde during descent

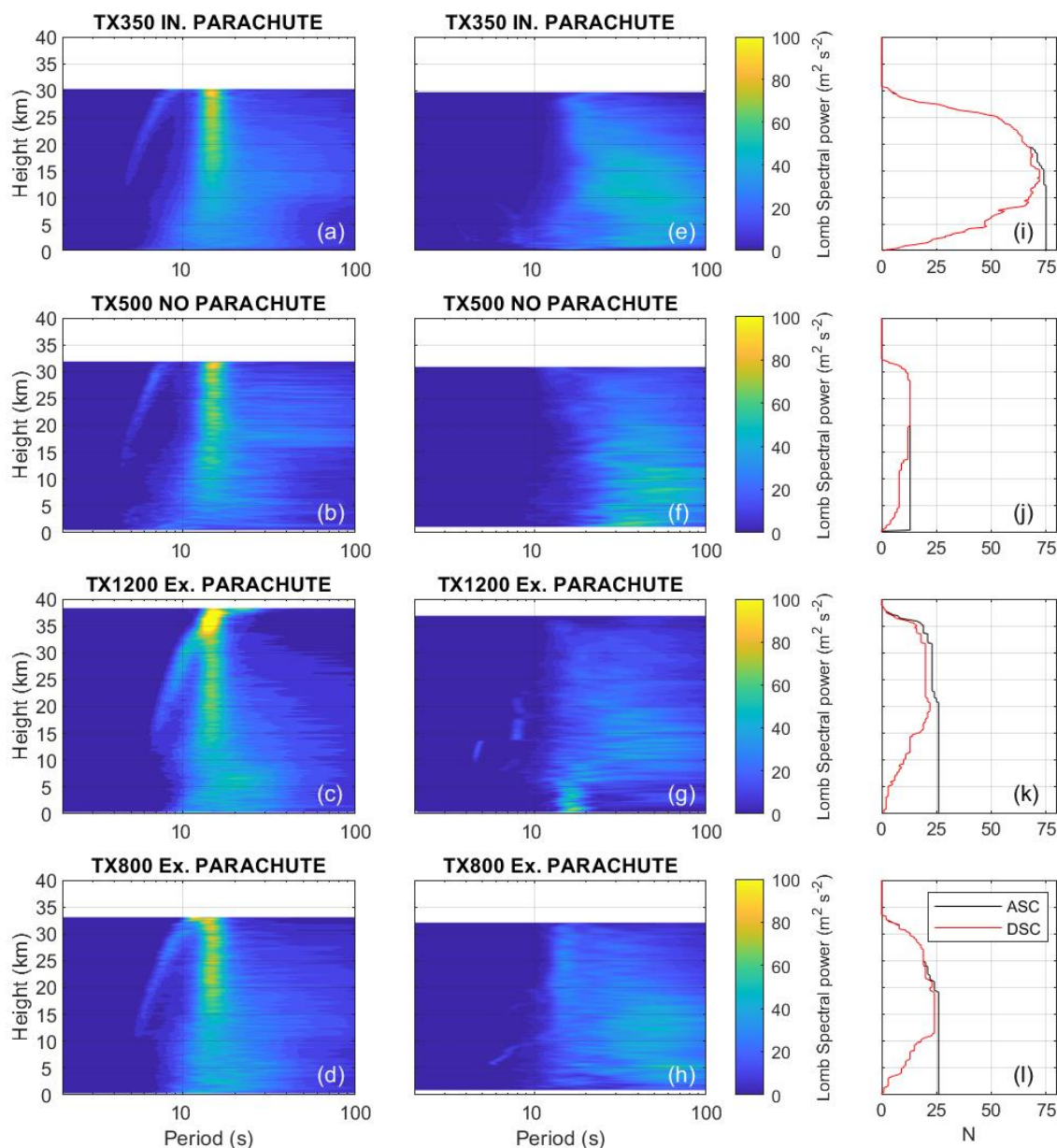
176 A radiosonde as it ascends through the atmosphere can be thought of as a pendulum with a moving pivot (Marlton et al, 2015).
177 As the radiosonde encounters small scale turbulence which is ubiquitous in our atmosphere it causes the radiosonde beneath
178 to swing. The periodicity τ is a function of string length l given by

$$179 \tau = 2\pi \sqrt{\frac{l}{g}}, \quad (1)$$

180 where g is the acceleration due to gravity. Different radiosonde manufacturers supply different string lengths to their
181 radiosondes, with the aim of removing the radiosondes sensors from the wake effects (Luers & Eskridge 1998). The standard
182 string length on the Vaisala RS41 is 55 m (Vaisala 2017) which gives an approximate period of oscillation 14.9 seconds and
183 an oscillating frequency of approximately 0.06 Hz. Differing balloon sizes and the inclusion of a parachute may alter l and
184 therefore τ slightly, a +/- 5m variation of l affects τ by +/- 0.6 s. Depending on the operating practices the radiosonde may be
185 launched in three broad configurations: i) No parachute; the radiosonde freefalls with some drag from the balloon remnants,
186 ii) Balloon bursts above the parachute and radiosonde descends on the parachute and iii) The balloon contains a parachute
187 which then deploys above the neck of the balloon and similarly descends. In addition to this, the deployment of the parachute
188 is not consistent, see Figure 5 and Figures S3 and S4 in the supplemental material.

189
190 Marlton (2016) performed a spectral analysis of raw GPS wind measurements from Vaisala RS92 radiosonde ascents equipped
191 with motion sensors described in Harrison and Hogan (2005) and Marlton et al (2015) and found oscillatory modes detected
192 by the motion sensors were present in the raw GPS data. In this section raw GPS ascent and descent data from UK Met Office
193 Autosonde sites and manned stations are used to generate Lomb Periodograms of the raw horizontal wind components.

194
195 Due to radiosondes often travelling 4-5 times their vertical ascent height in the horizontal there are on occasion small data gaps
196 due to transmission drop out. The issue becomes more noticeable in descent data as the radiosonde is now even further from
197 its ground station. This means a traditional Fourier transform method is not appropriate. Thus, a Lomb periodogram is chosen
198 (Lomb 1979), which can generate periodograms which have irregularly sampled data. To ensure that we focus on the motion
199 of the radiosonde we use the processed horizontal wind components to remove the wind field from our raw GPS readings
200 leaving the motion of the radiosonde beneath that balloon.



201

202 Figure 8. Composite Lomb Periodograms of detrended horizontal GPS data as a function of height for ascent data from RS41's
203 with the following launch configurations a) TX350 balloon with internal parachute, b) TX500 with no parachute, c) TX1200
204 with external parachute (day time only) and d) TX800 with external parachute. Panels e-h show composite Lomb periodograms
205 of descent data from the balloon configurations a-d respectively. Profile contributions for balloon configurations a-d during
206 ascent (descent) are shown in black (red) in panels i-l respectively.

207



208 Figure 8 a-d shows Lomb periodograms of the detrended horizontal GPS during an ascent for four different RS41 launch
209 configurations, in each case there is a dominant oscillatory period of 15 s (0.06 Hz) which strongly dominates above 15 km.
210 Examining the results from Eq (1) given the RS41's string length shows that on ascent the radiosonde and balloon are behaving
211 as a pendulum with a moving pivot.

212

213 During descent the oscillatory motion is very different, there is no longer a dominant oscillatory period and the amplitudes of
214 these oscillations are smaller. A general trend is that in the early stages of the descent the radiosonde is still oscillating with a
215 period of 15 s (0.06 Hz). As it falls the peak period of oscillation increases to 25-30 s, until the height of 15-20 km. At this
216 approximate height the non parachuted RS41s (panel (e)) exhibit a narrow spectral width with the smallest descent to descent
217 variability. An oscillation is still present indicating that some of the balloon remnants are acting as a parachute. For the
218 parachuted RS41s the spectral width in oscillation widens significantly indicating that there is variation in the motion behavior
219 of the radiosonde. As discussed earlier this may be due to how and when the parachute deployed and if any of the parachute
220 remains entangled with the parachute rigging. The latter is hard to determine without retrieving the radiosonde which is seldom
221 done. We can get a better understanding of the variation in oscillation by looking at individual ascents.

222

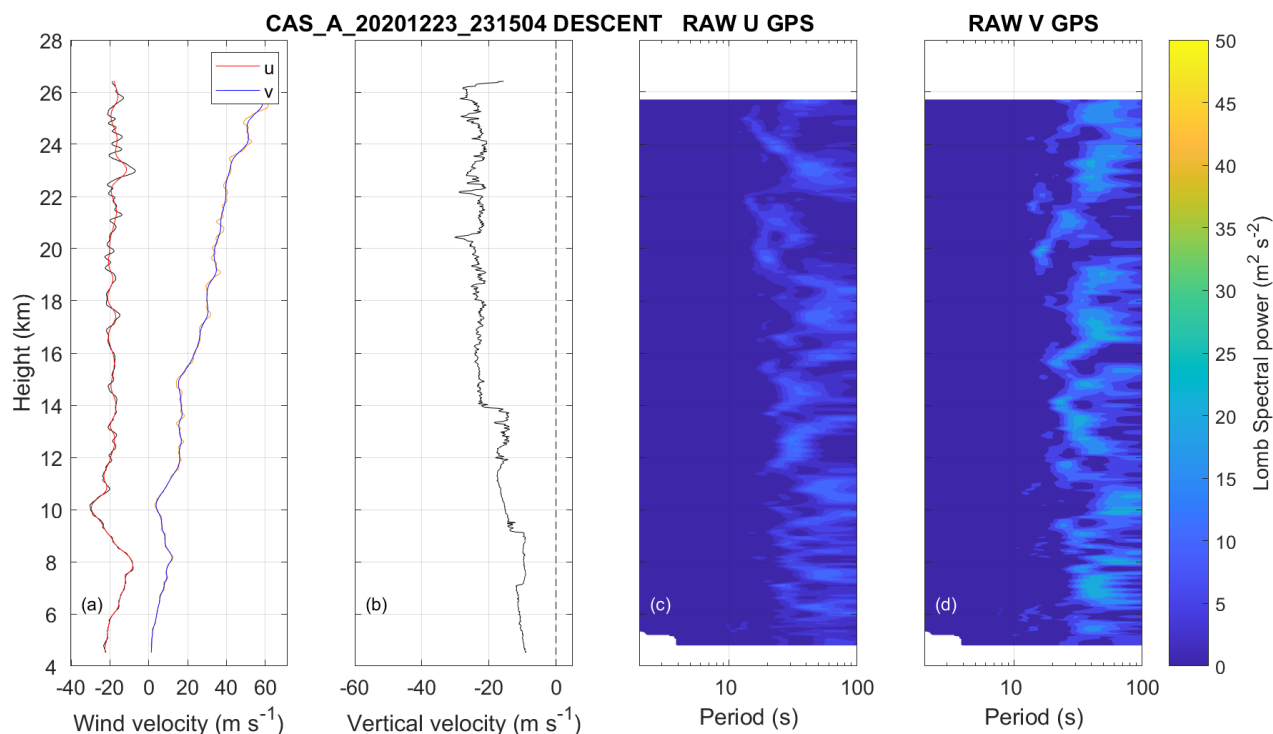
223 Figure 9 and Figure 10 show two descents from Castor Bay Autosonde station (54.50 N, 6.34 W). In both figures panel a
224 shows the processed horizontal wind components u and v components in red and blue respectively. The raw GPS wind
225 components are shown in black and orange for the u and v components respectively. Panel b shows the descent speed and c
226 and d show Lomb periodograms of the detrended raw GPS velocities. In Figure 9 we can see that the parachute does not seem
227 to offer significant deceleration to the sonde until about 14 km. During the descent there are weak low frequency oscillations
228 greater than 60 seconds over the duration of the ascent. In panel figure 9a the raw GPS and the processed v component of the
229 wind track very closely and it is hard to differentiate between them. Figure 10 is a descent from a different day which tells a
230 very different story. The parachute deploys within 1 km of the burst height and causes a sudden deceleration from -60 m s^{-1} to
231 -20 m s^{-1} . After the rapid deceleration the radiosonde enters a high amplitude oscillatory mode with a periodicity of 30-40
232 seconds as it descends. A hypothesis here is that the sudden deceleration caused by a correct deployment of the parachute has
233 caused the oscillatory mode seen here. The amplitude of oscillations seen under this scenario could introduce error in the
234 processed winds and is a possible area for future study.

235

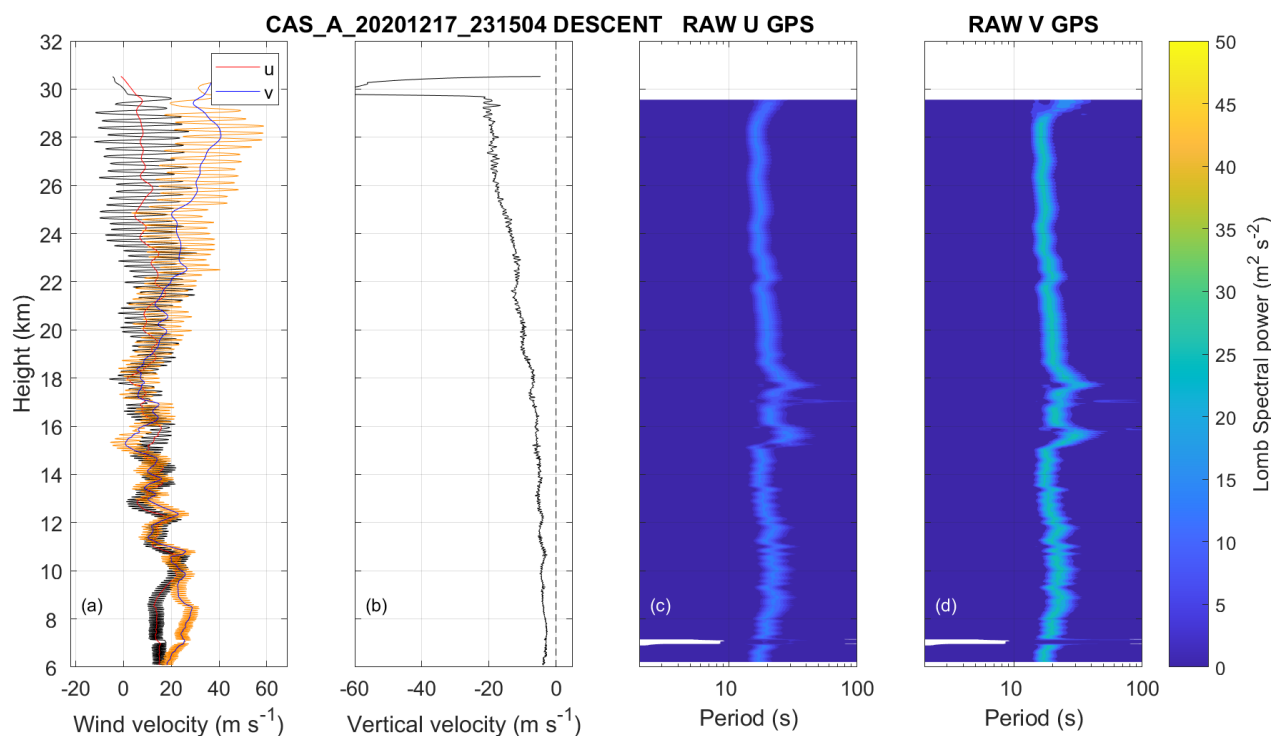
236 Here it has been shown that identical balloon configurations have very different and random descent characteristics. Figure 4
237 shows that the balloon sometimes intertwines itself about the parachute which may affect how well the parachute deploys and
238 in turn its oscillatory characteristics on descent. A successful parachute deployment can enhance the oscillation such that it
239 has potential to introduce error in descent wind data. More research in this area needs undertaking using an approach where
240 motion sensors are attached to the RS41 to better understand the descent to descent variability. Additional investigations where
241 guillotines cut the balloon from the parachute such as that used on heavy scientific balloon payloads, could be utilised to



242 remove the effect of balloon entanglement. The placing of a small central hole in the top of the parachute to improve stability
243 and removal of sudden deceleration also need investigating.
244



245
246 Figure 9. Vertical profiles of a) processed horizontal wind components u and v in solid red and blue respectively with raw
247 GPS winds in black and orange for the u and v components respectively, and b) descent speed. Panels c) and d) show Lomb
248 periodograms of the detrended raw GPS velocities as a function of height for a sounding made at Castor Bay autosonde station
249 (54.50 N, 6.34 W) at 2315UT on 23/12/2020.



250

251 Figure 10. Vertical profiles of a) processed horizontal wind components in solid red and blue for u and v respectively with
252 raw GPS winds in black and orange for u and v respectively, and b) descent speed. Panels c) and d) show Lomb periodograms
253 of the detrended raw GPS velocities as a function of height for a sounding made at Castor Bay Autosonde station (54.50 N,
254 6.34 W) at 2315 UTC on 17/12/2020.

255

256 In summary, ascending radiosondes tend to have similar characteristics in terms of motion beneath the balloon and ascent
257 speeds, although the latter does depend on the amount of gas within the balloon. Descending radiosondes have widely varying
258 descent characteristics which are due to the random nature of how the balloon and parachute interact (if present) and how
259 effective the parachute is at slowing the balloon. The motion on descent may be more consistent if the radiosonde could be
260 'cut free' of the balloon remains and fall on its own without a parachute. It would be interesting to study the effect of cutting
261 the string just after balloon burst, but this may be technically difficult and the risk associated with the radiosonde falling at
262 terminal velocity would need to be assessed. Given the variation in burst heights, reliably cutting it before burst would reduce
263 the average height attained. In addition similar motion and orientation sensors as used in Harrison & Hogan (2004) and Marlton
264 et al. 2015 could be used to ascertain more information about the orientation of the descending radiosonde package

265



266 **3 Comparison with ECMWF background fields**

267 **3.1 ECMWF forecasting system**

268 For comparison we use statistics from the ECMWF operational data assimilation system for September to November 2019.
269 The forecast model had a horizontal grid spacing of about 9 km and 137 levels in the vertical and the assimilation used 4DVar
270 with a 12 h window. The 3...15 h forecast from the previous analysis forms the background for the assimilation and the
271 observation-minus-background (O-B) statistics can yield a lot of information. The background values are not perfect but
272 provide a relatively accurate and (generally) independent estimate of the measured variables. In many respects the forecasting
273 system is similar to that of ERA5 (Hersbach et al, 2020) which was based on the operational system of 2016. One difference
274 from ERA5 is that treatment of radiosonde drift was introduced operationally in June 2018 and this improved upper-level O-
275 B standard deviations by 5-10% (Ingleby et al, 2018). Prior to this radiosonde profiles were treated as vertical and
276 instantaneous, afterwards the profiles were split into sub-profiles of 15-minutes each and treated as valid at time and
277 latitude/longitude of the first point in the sub-profile. Descent profiles are split into 5-minute sub-profiles for comparison with
278 the model.

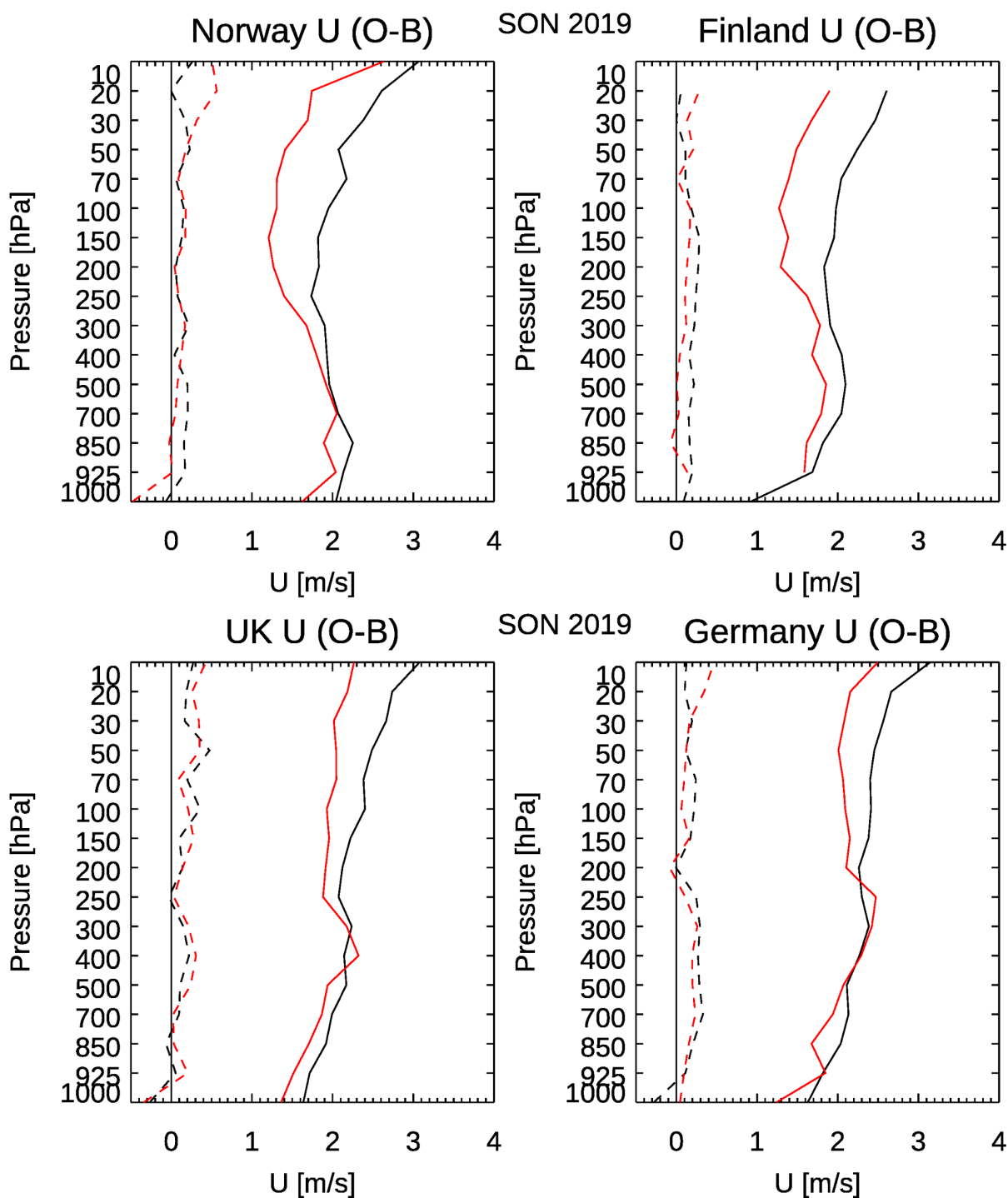
279 **3.2 Wind comparison**

280 Figure 11 shows mean and standard deviation (SD) profiles of O-B differences at radiosonde standard levels for the u (zonal)
281 component of the wind. The statistics for the v (meridional) component are similar and are not shown. The mean differences
282 (dashed lines) are close to zero, as hoped. The standard deviations are approximately 2 m s^{-1} , but are slightly larger at the top
283 levels. One surprise was that the descent profiles (in red) fit the background more closely than the ascent profiles (in black),
284 particularly at upper levels. Comparing individual ascent/descent profiles the descent winds generally appear smoother and
285 this appears to be the cause of the better fit to background. Figure 12 shows the raw 1-second data for a single profile (faint
286 line) and the data after smoothing to remove the pendulum motion (bold line). In this case the smoothing was performed using
287 the GRUAN algorithm (Dirksen et al, 2014), whereas the BUFR reports have smoothing applied by Vaisala MW41 software
288 which is similar but not identical. In both cases the smoothing is a time filter applied to ascent and descent data in the same
289 way. The period of the pendulum motion depends on the length of the pendulum which will be approximately the same for a
290 parachute as for the balloon. (Of course, if there is no parachute there is a different scenario for the descent.) Because the
291 radiosonde is falling faster than it ascended, a filter based on a fixed time interval corresponds to a larger height interval on
292 the descent. Note also that the MW41 processing does not include an inertial correction as used in the AVAPS dropsonde
293 processing (Sect. 1), this counteracts time-lag effects which will be largest when falling fastest. As shown in Figure 12, at
294 most levels there is less high frequency 'pendulum' motion on the descent - although at the top levels there can be substantial
295 amounts of noise.

296 Figure 13 shows SD(O-B) for individual descents in the interval 30-50 hPa against the mean descent rate for this pressure
297 range. The standard deviations are slightly larger for slower descent rates, this is thought to be linked to more pendulum motion



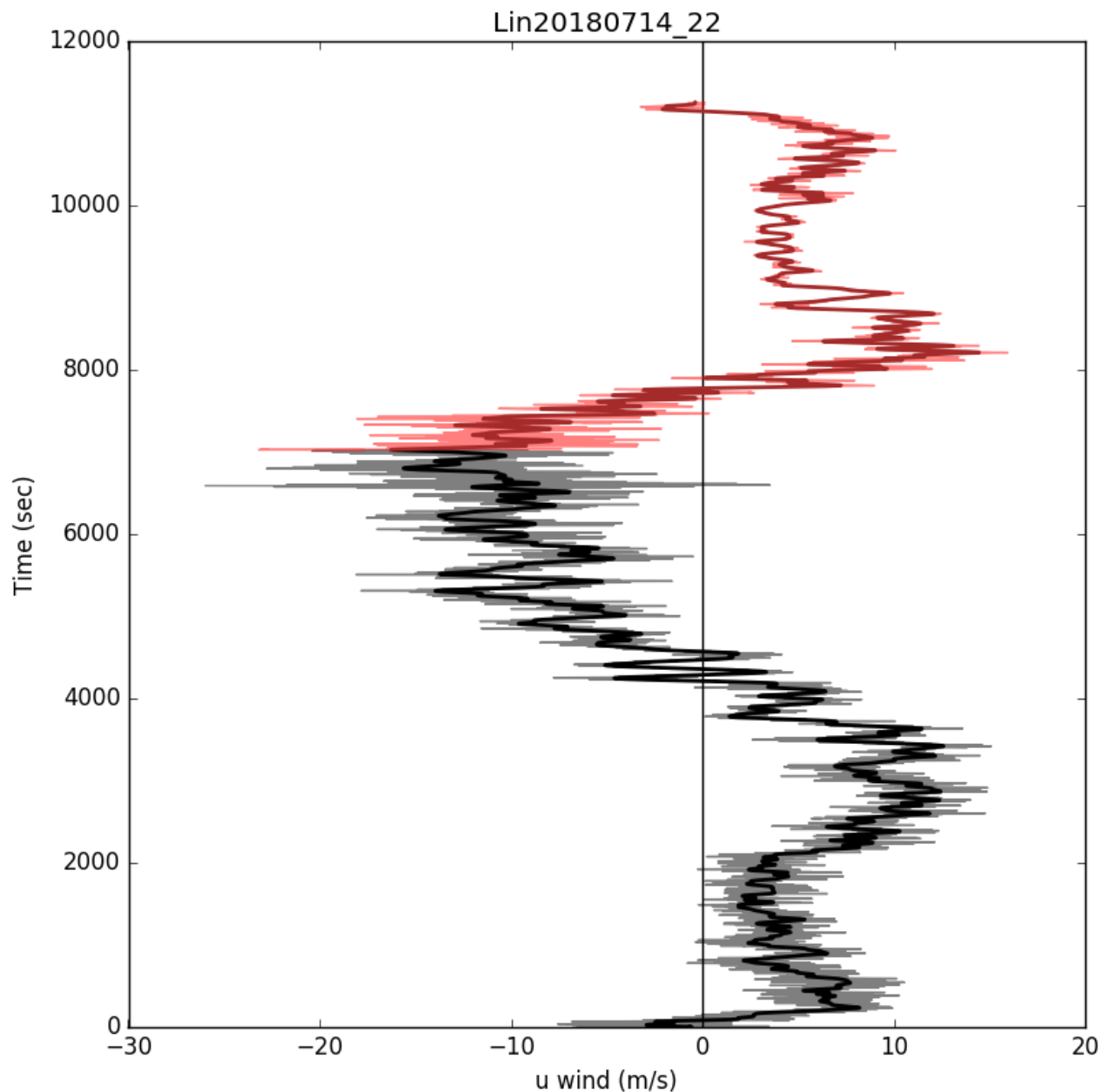
298 when the parachute is slowing the descent more effectively. Similar effects can be seen for other pressure ranges, but there is
299 no clear dependence of the mean (O-B) winds on descent rate (not shown).



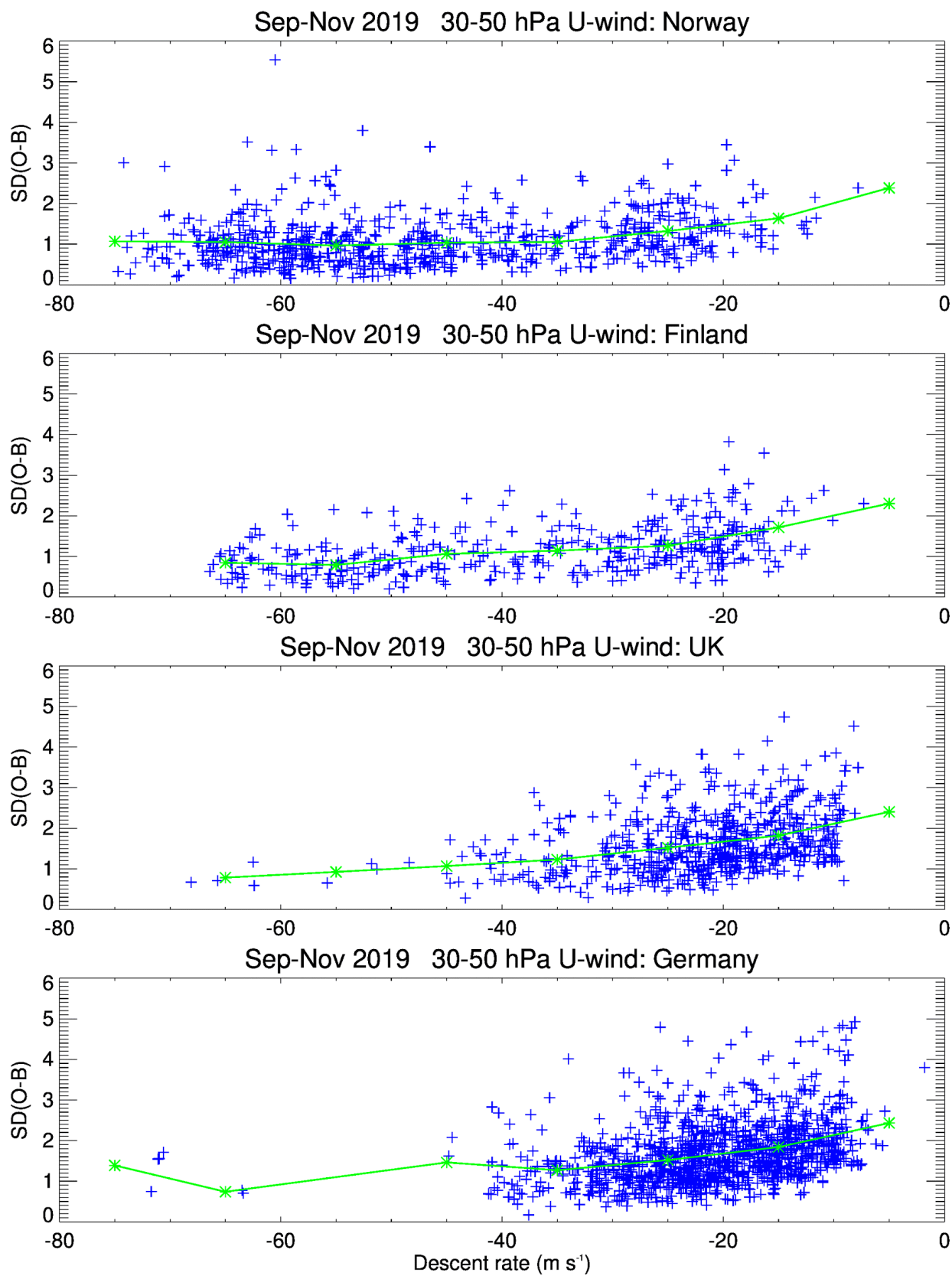
300



301 Figure 11. U-component standard level statistics of mean (dashed) and SD (solid) O-B differences for ascent (black) and
302 descent (red) for four different countries, September - November 2019.



303
304 Figure 12. Raw (1-second) data (pale line) and filtered (bold line) u component as a function of time: ascent (black) and
305 descent (red). This is for a launch from Lindenberg, including a parachute for the descent.





307 Figure 13 Standard deviation of (O-B) plotted against mean descent rate, both for descents from 30 to 50 hPa (blue symbols).
308 The green symbols show average values for bins of 10 m s⁻¹.

309 3.3 Temperature comparison

310 Firstly, we note that at about 50 hPa, in the extratropics, the ECMWF background is too cool by about 0.5°C (this can be seen
311 against the RS41 ascent data in Figure 14). This is recognised as a model error, due mainly to excessive humidity and hence
312 extra long-wave cooling as shown by Shepherd et al (2018). More recent work on the analysis system has approximately
313 halved the short-range forecast bias (Laloyaux et al., 2020). To provide reassurance ascent/descent pairs were compared to
314 radio occultation (RO) retrievals (Table 2). The RO data (Laloyaux et al., 2020) is much closer to the ascent temperatures than
315 the descent temperatures - note that the sample size is much smaller than for the O-B statistics.

316

Pressure (hPa)	Sample	Ascent-RO (°C)	Descent-RO (°C)	Ascent-B (°C)	Descent-B (°C)
5	22	-0.07	1.07	-0.37	0.90
10	36	0.53	1.63	0.25	1.25
20	125	0.13	1.04	0.37	1.33
30	130	0.15	0.92	0.45	1.24
50	135	0.02	0.37	0.44	0.84
70	137	-0.11	0.17	0.39	0.68
100	136	0.28	0.41	0.31	0.51

317

318 Table 2. Collocations with radio occultation retrievals (within 100 km and 2 hours) at standard levels, with mean temperature
319 differences (°C). Columns show Radiosonde Ascent (or Descent) minus RO or Background values.

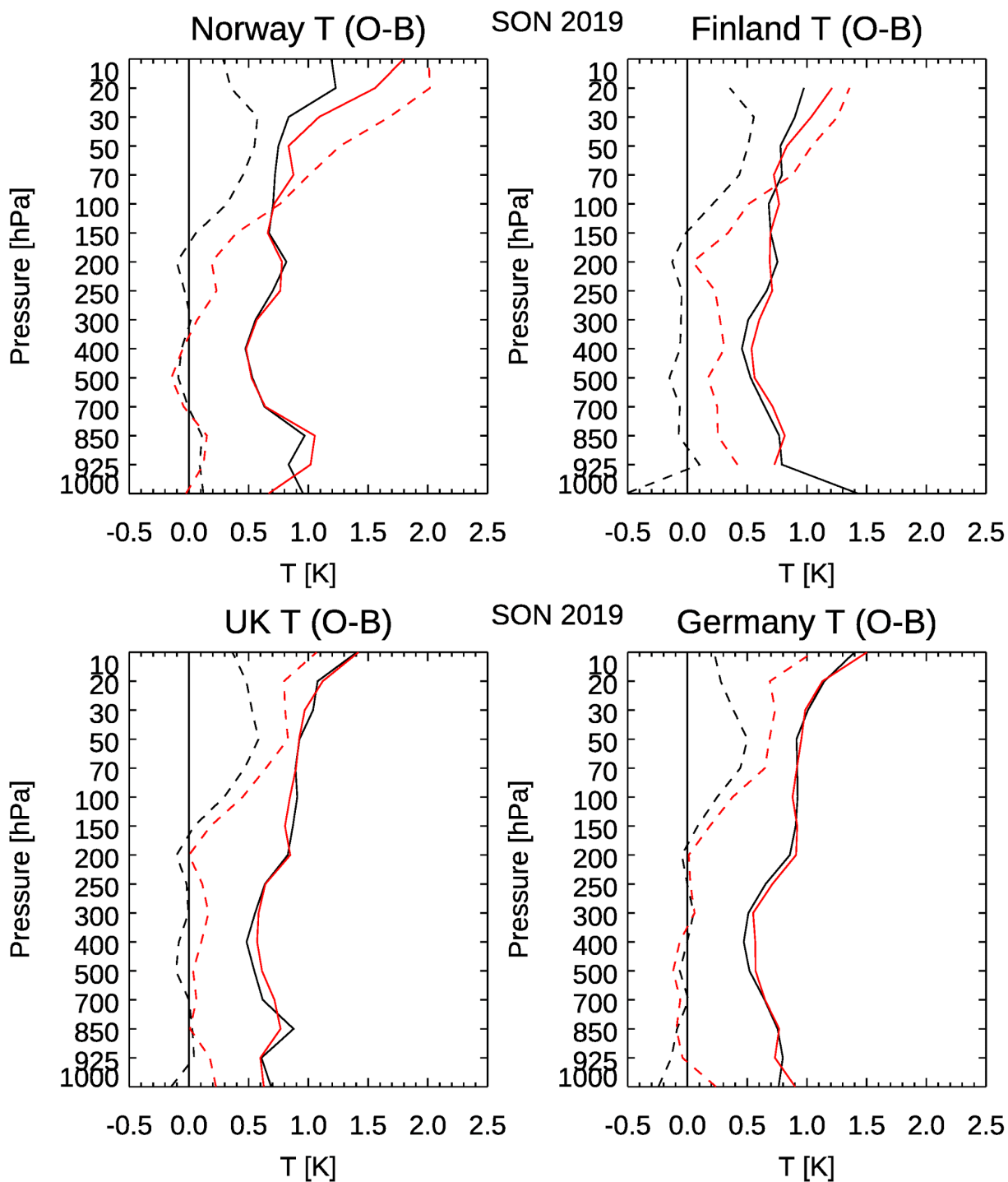
320

321 The clearest difference between ascent and descent is that at upper levels the descent temperatures are higher than the ascent
322 values (Figure 14). This has been noted previously, for different radiosonde types, see section 6. At 10 hPa the descent-ascent
323 difference is over 1.5°C for the Norwegian stations and about half that for the UK and German stations. For Finland the
324 highest standard level reached is generally 20 hPa and the difference there is about 1°C. One hypothesis advanced was that
325 this could be a time-lag effect. However, descending from 30 to 100 hPa the mean temperatures were approximately constant
326 or increasing slightly (Figure 15) suggesting that another explanation is needed. A convincing link to the radiosonde fall speed
327 was found (Figure 16). There is no clear link to the time of day (and solar radiation) as shown by the different coloured
328 symbols in Figure 16. The fall rate correction put forward in the next section (derived originally for a single radiosonde station)
329 does a good job of removing most of the bias (Figure 17). The SD(O-B) for temperature shows no clear link to fall rate (not
330 shown).

331 Returning to Figure 14 the large top-level ascent-descent difference in the Norwegian data has disappeared by 300 hPa, but
332 the smaller top-level Finnish difference becomes an offset of 0.2 or 0.3°C throughout the troposphere. The important
333 difference seems to be that the Norwegian radiosondes have a pressure sensor, but the Finnish radiosondes do not. Without a

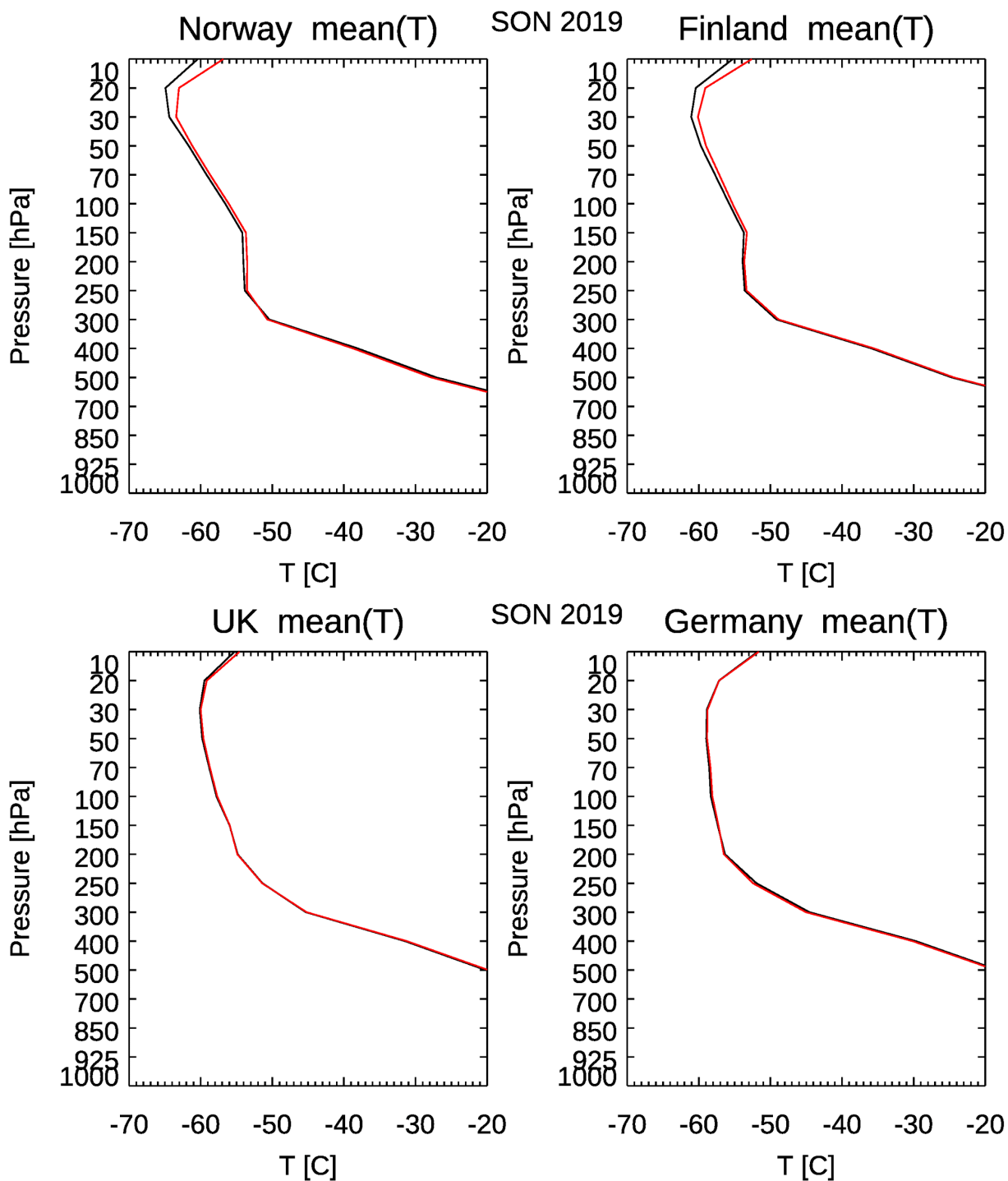


334 pressure sensor the pressures must be computed and biases in the temperature will feed into later biases in the pressures -
335 discussed in more detail in the next section. A smaller version of the same effect can be seen between the German data (with
336 pressure sensors) and the UK data - without a pressure sensor these have an offset of about 0.1°C in the troposphere: smaller
337 than the Finnish data because the UK radiosondes have parachutes.



338

339 Figure 14. As figure 11 but for temperature.

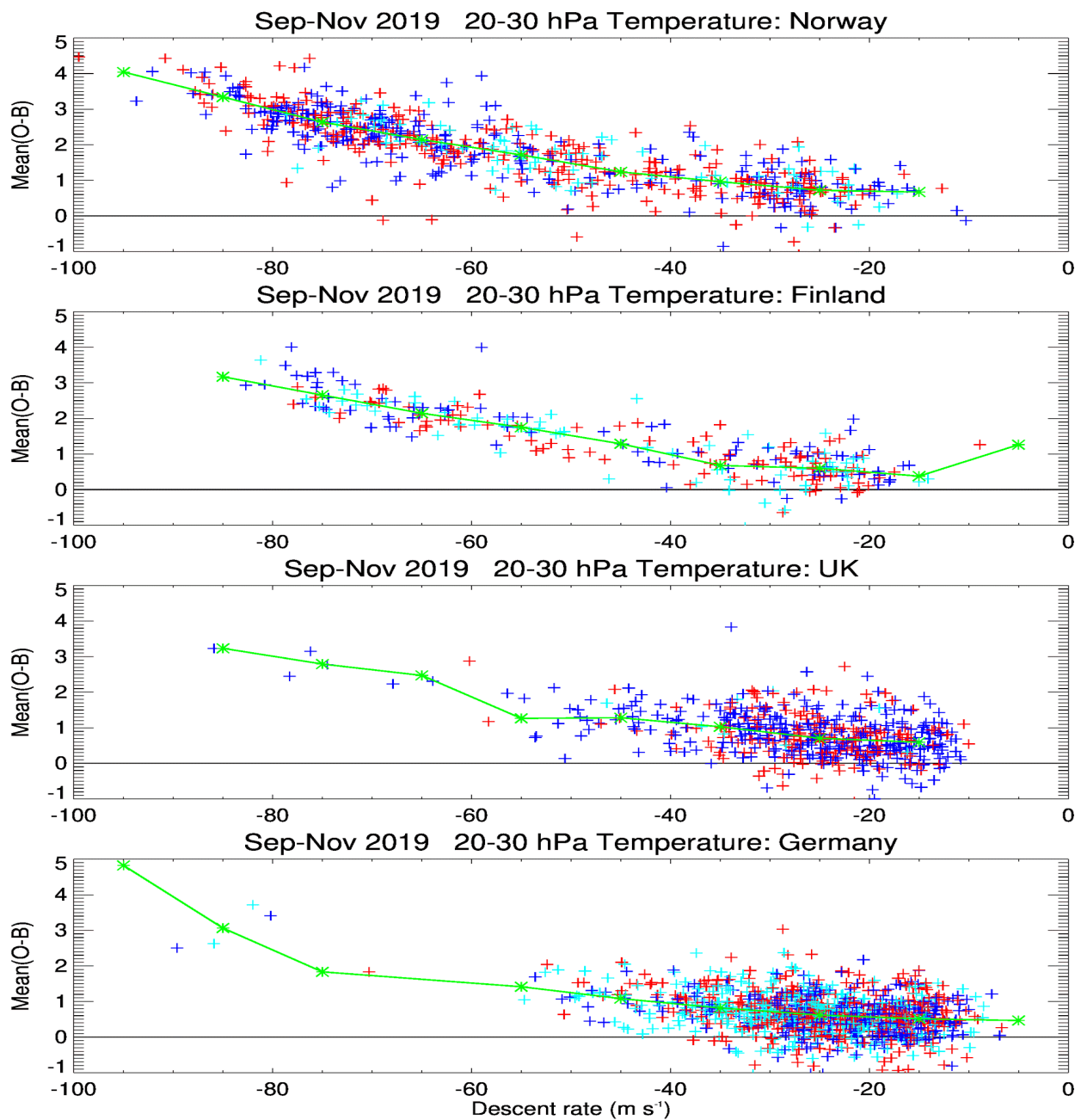


340

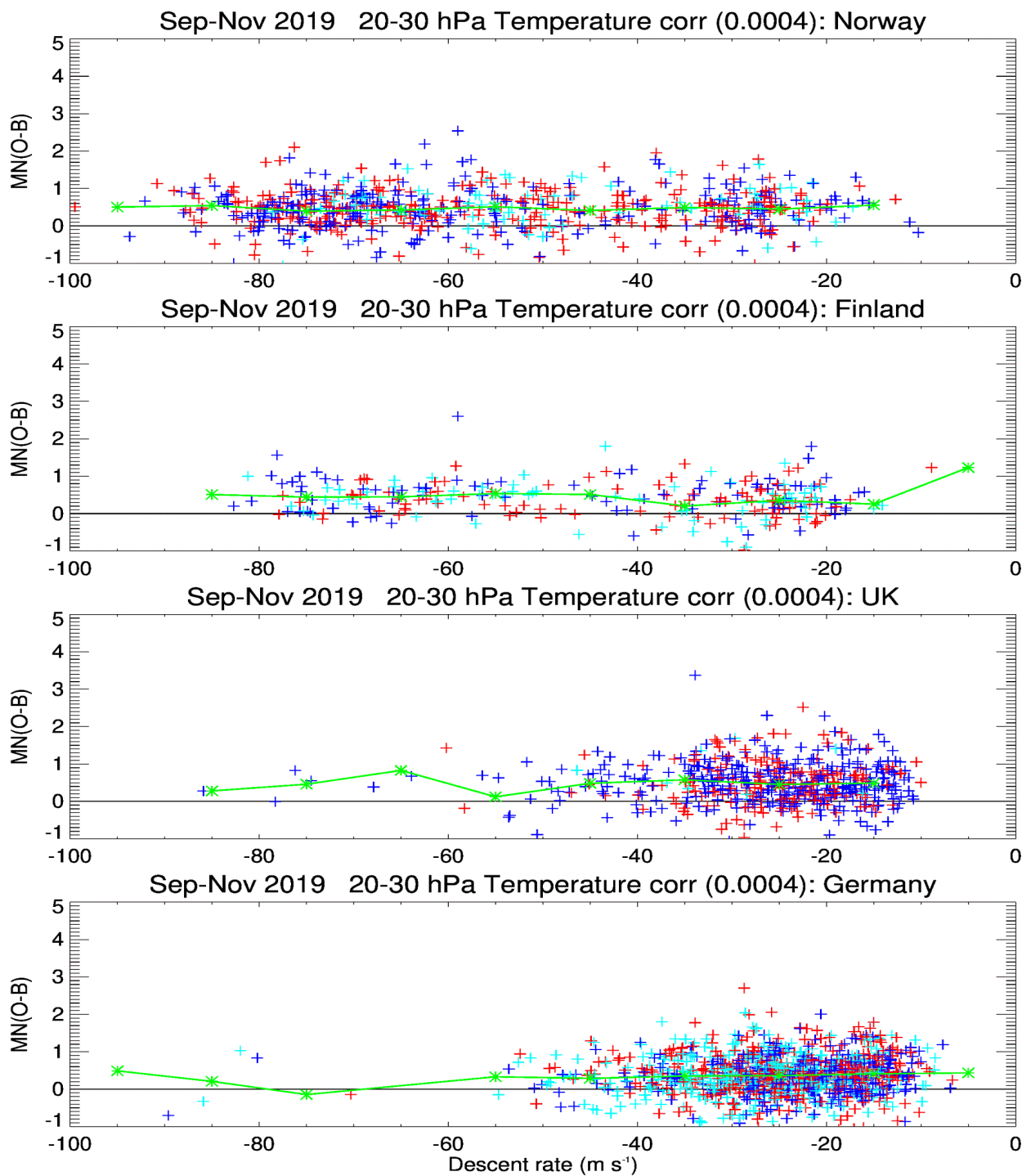
341

342

Figure 15. Mean ascent and descent temperatures at standard levels - range chosen to emphasise upper levels. Particularly above 30 hPa the locations sampled will be from a smaller subset of profiles/stations.



343
344 Figure 16. Comparison between mean fall speed from 20 to 30 hPa and mean O-B temperature. Red markers denote nominal
345 12 UTC profiles, dark blue markers nominal 00 UTC profiles and cyan denotes intermediate profiles. (Recall that the B values
346 have a bias of about 0.4°C at these levels.) Green markers show values averaged over all times of day in bins of 10 m s⁻¹.



347

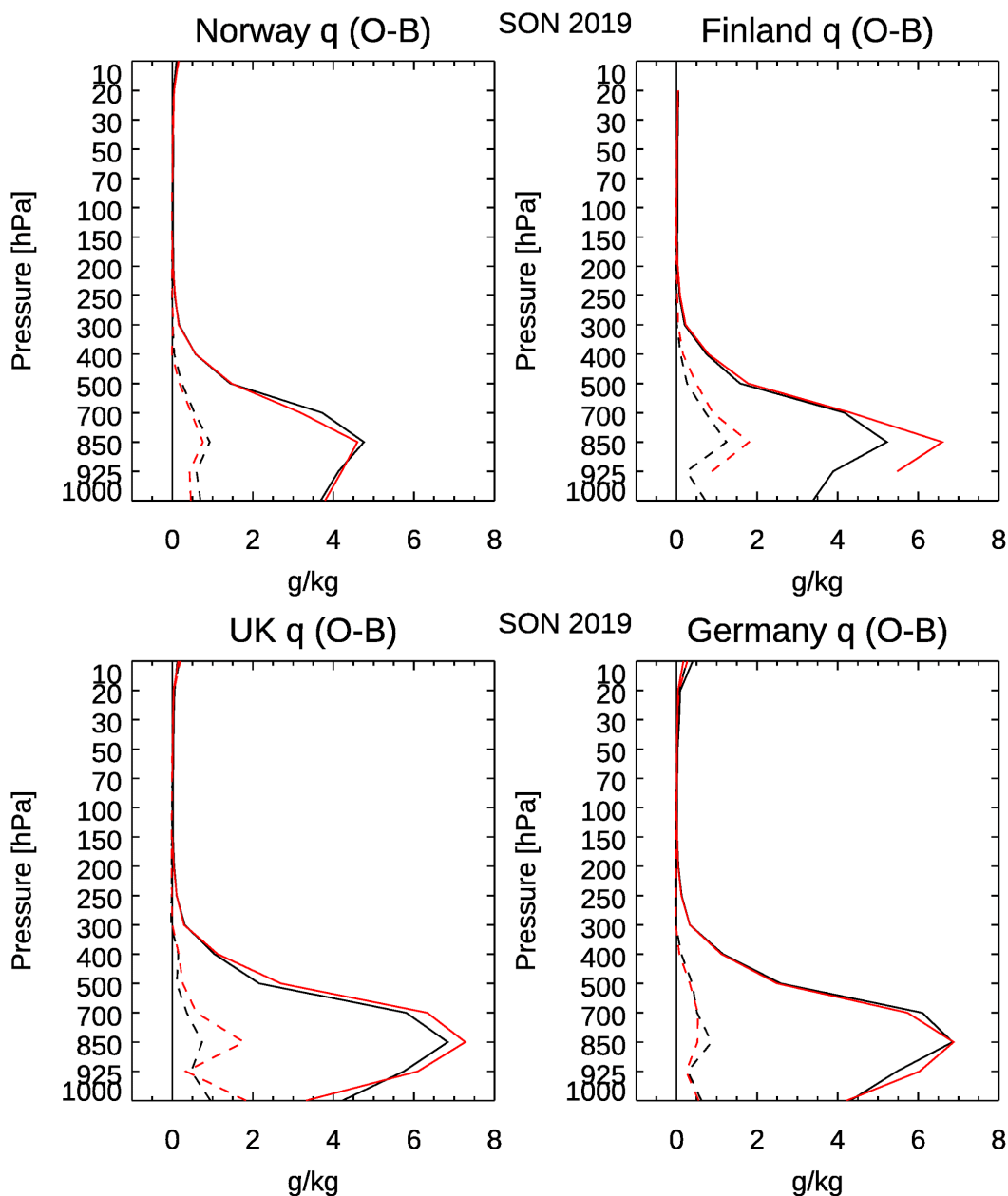
348 Figure 17. As Figure 16 but temperatures adjusted as described in section 4.1 (with $A=0.0004$).



349 **3.4 Humidity comparisons**

350 Figures 18 and 19 show ascent/descent comparisons with the background for specific and relative humidity (RH). Broadly
351 speaking the ascent and descent statistics are very similar, although the descent fit to background is slightly worse for the
352 Finnish radiosondes in the troposphere. Between about 50 and 150 hPa the SD(O-B) for RH is smaller for the descent, but
353 note that stratospheric radiosonde humidity is not assimilated in the ECMWF or other NWP systems.

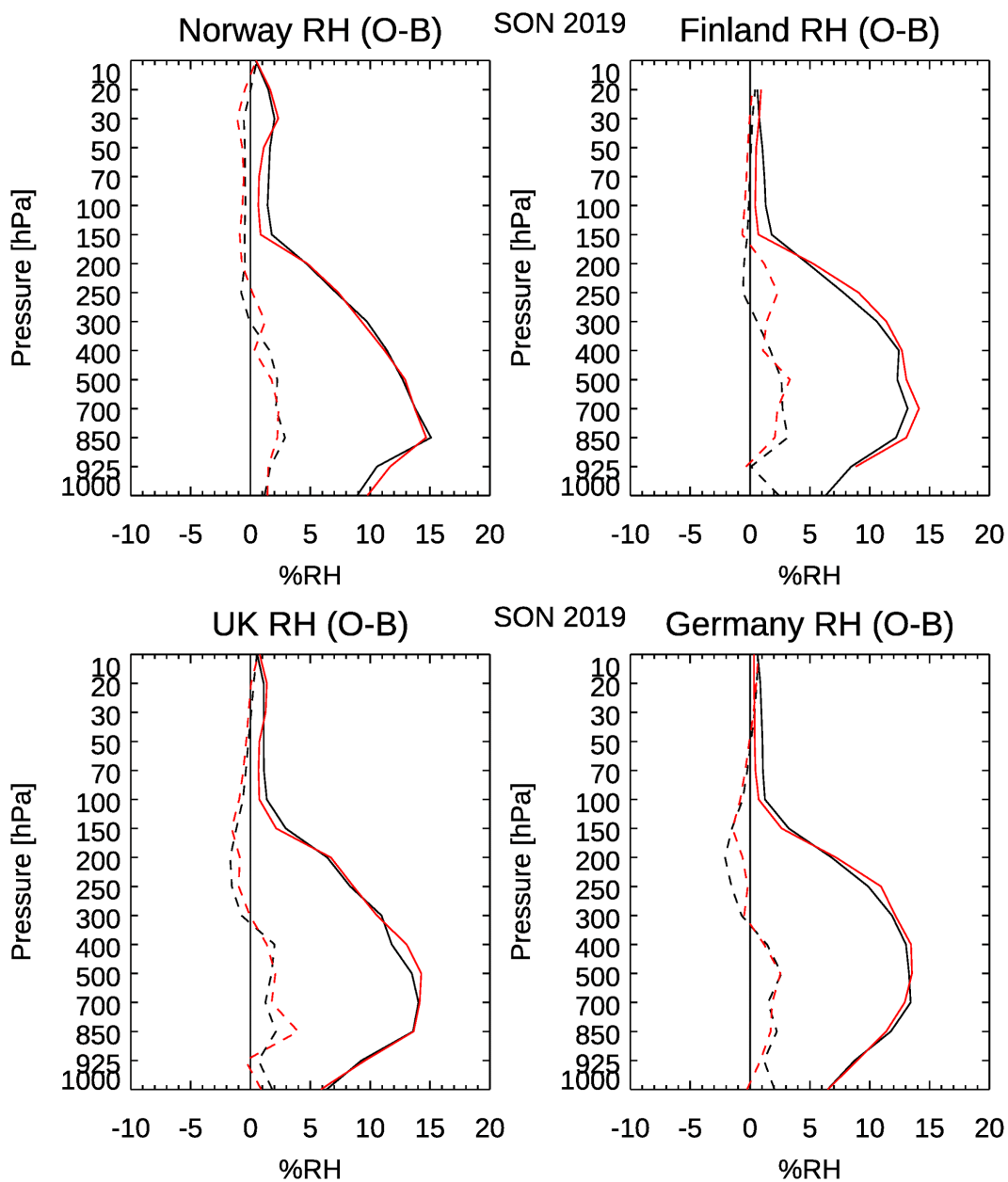
354



355



356 Figure 18. As figure 11 but for specific humidity.



357
358 Figure 19. As figure 11 but for relative humidity.
359



360 4 Warm bias during descent

361 4.1 Direct effect of heating

362 As the comparison of descent data with NWP model suggests, there is a positive temperature bias for the data measured by
363 descending Vaisala RS41 radiosondes. This bias is bigger in the stratosphere than in the troposphere and is more significant
364 for the data taken from radiosondes without parachutes.

365 As the descent rate often exceeds 50 m s^{-1} , occasionally even 100 m s^{-1} , frictional heating seems to be a reasonable explanation
366 of the observed bias. A related issue is recognized for sensors on aircraft, which also measure temperature while moving with
367 high speed relative to the free air (WMO 2018b, section 3.3). For aircraft the kinetic energy is transferred to internal heat
368 mostly by adiabatic compression. In the case of radiosondes we expect that most of the conversion is done by direct collisions
369 of air and sensor molecules (friction), but it is also possible that the effect is done by adiabatic compression in the boundary
370 layer of the sensor. We use a quadratic relationship on descent rate (DR) - this arises from a simple energy balance, independent
371 of the energy conversion mechanism:

$$372 \Delta T = A \cdot DR^2 \quad (2)$$

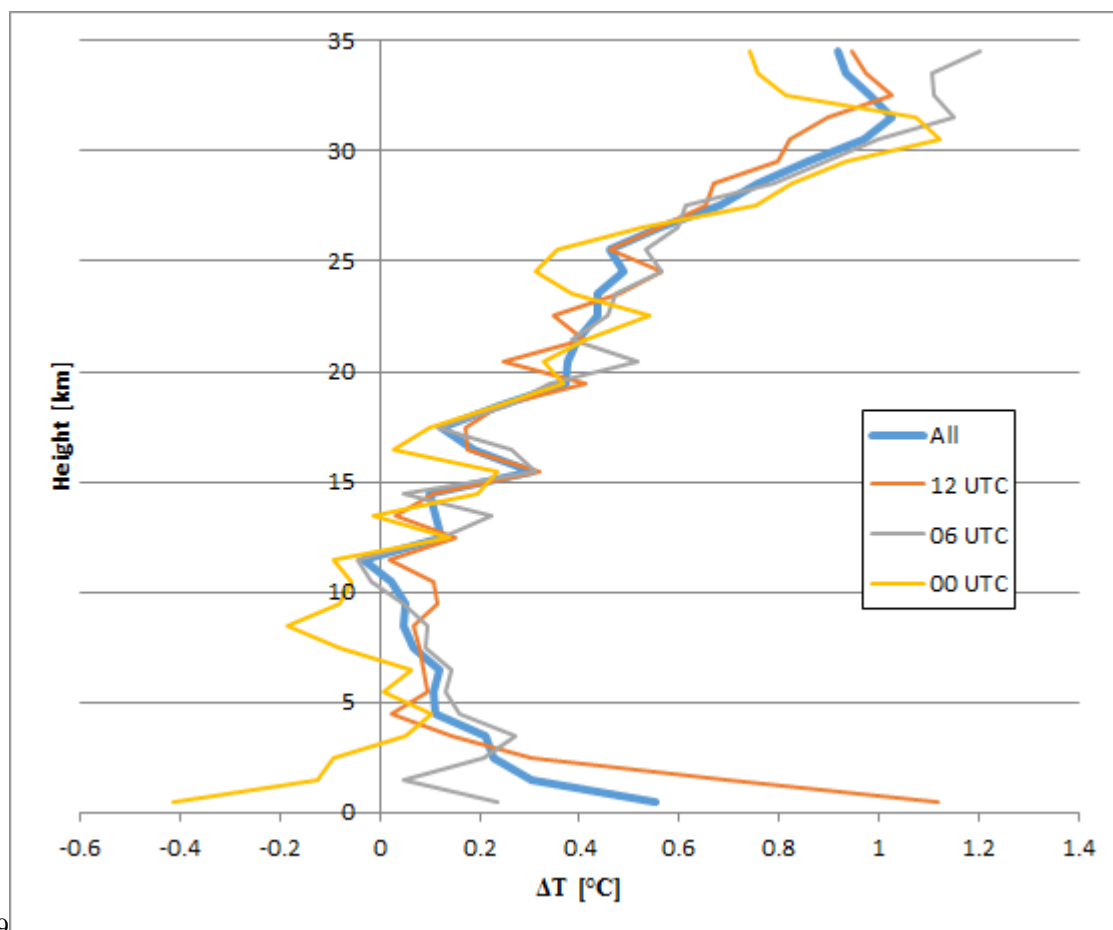
373 A is a coefficient, determined below. This is similar to the equation for the heating of aircraft temperature sensors - see
374 Appendix. It is also linked to the ‘viscous dissipation’ or ‘compressional heating’ mentioned by Wagner (1964) for
375 rocketsondes (launched high in the atmosphere by a rocket they measure on the descent, slowed by a parachute). This
376 relationship was examined by comparing the descent temperatures with ascent temperatures from the same radiosonde. Most
377 of the data were from the Praha-Libus (Prague) upper air station: 554 descents with average length of descent 23 km. From
378 these data there was a sample of about 528 000 comparable levels. The data covers the period from July 2019 to January 2020.
379 This station used radiosondes RS41-SG, without pressure sensor or parachute - so similar to the soundings from Finland in
380 section 3.

381 The time and space difference between ascent and descent measurement of a particular level starts at 0 km and seconds at the
382 moment of balloon burst and can rise up to 2 hours and 150 km for lower troposphere levels. We expect that this difference
383 will result in deviations of atmospheric measurements, but according to the long-term data there wasn’t expected any bias
384 caused by this difference in the stratosphere. For the lowermost layers (below 4 km) was expected warm bias for 06 and 12
385 terms, and cold bias for 00 term due to the diurnal variation.

386 For each level of descent was taken height (H), descent rate (DR) and descent temperature (T_D), with ascent temperature (T_A)
387 interpolated to this level. After dividing the sample into groups of 1000 m the bias was calculated (mean temperature difference
388 $\Delta T = T_D - T_A$) for each of these groups. Results shown in Figure 20 are very similar to comparison of German data shown in
389 Figure 14 – about 1°C bias at the highest levels decreasing to 0°C at 12 km. A positive bias near the surface is an expected
390 effect of diurnal variation and after separating data into 00, 06 and 12 UTC groups, the differences seen are approximately -
391 0.4°C , 0.2°C and 1.1°C respectively.



392 According to equation [2], ΔT should depend solely on DR. Pearson's correlation coefficients confirms the strong link between
393 those two variables. It was 0.21 between ΔT and H, between ΔT and DR it was 0.40.



394 9
395 Figure 20. Temperature differences between ascent and descent as a function of height (Praha-Libus data).

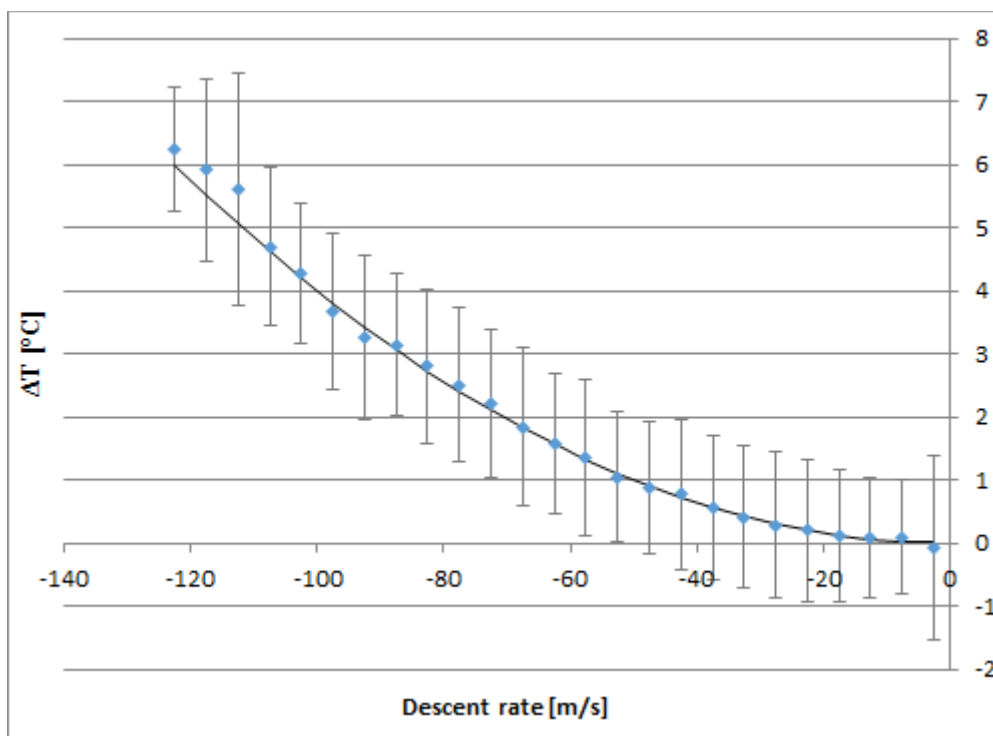
396
397 In the next step the sample was binned by DR – intervals used were 0-5 m/s, 5-10 m/s etc. There is clearly a quadratic
398 dependence of ΔT on DR in Figure 21 (average ΔT for these bins). The standard deviation of ΔT shown with grey lines is
399 almost independent of DR. The black line is the best estimate with $A = 4.05 \cdot 10^{-4}$.

400 For DR greater than 110 m/s the fit is slightly less good but the sample size is small with data available from less than 3 % of
401 examined soundings. When equation [2] with $A = 4.05 \cdot 10^{-4}$ is applied as a temperature correction, the root mean square ΔT
402 is lowered from 1.22 °C to 1.06 °C, indicating that the correction explains 24.4 % of the variance seen.

403 Calculating the correction as a complete quadratic equation ($\Delta T = 4.39 \cdot 10^{-4} \cdot DR^2 - 3.17 \cdot 10^{-3} \cdot DR + 5.40 \cdot 10^{-2}$), did not
404 significantly improve the result (explained variance increased by less than 0.01 %).



405 To find out if the result was affected by lower tropospheric differences (which are mostly caused by diurnal variation and not
 406 friction), the result was recalculated for the sample with all data below 4 km excluded. Results changed only very slightly
 407 again, the coefficient was then $A = 4.04 \cdot 10^{-4}$, and the explained variance increased to 25.3 %.



408
 409 Figure 21. Dependence of temperature differences between ascent and descent on descent rate, Praha-Libus.

410
 411 The coefficients were also calculated separately for the data from each time of the launch
 412 – 00, 06 and 12 UTC soundings – the estimates of coefficient A range from $3.9 \cdot 10^{-4}$ to $4.3 \cdot 10^{-4}$
 413 (Table 3).

Best estimate (at time, UTC) $\Delta T = A \cdot DR^2$	A [$^{\circ}\text{C} \cdot \text{s}^2 \cdot \text{m}^{-2}$]
00	$3.90 \cdot 10^{-4}$
06	$4.22 \cdot 10^{-4}$
12	$4.07 \cdot 10^{-4}$

414 Table 3. Best estimate of correction coefficient for different times of launch at Praha-Libus.

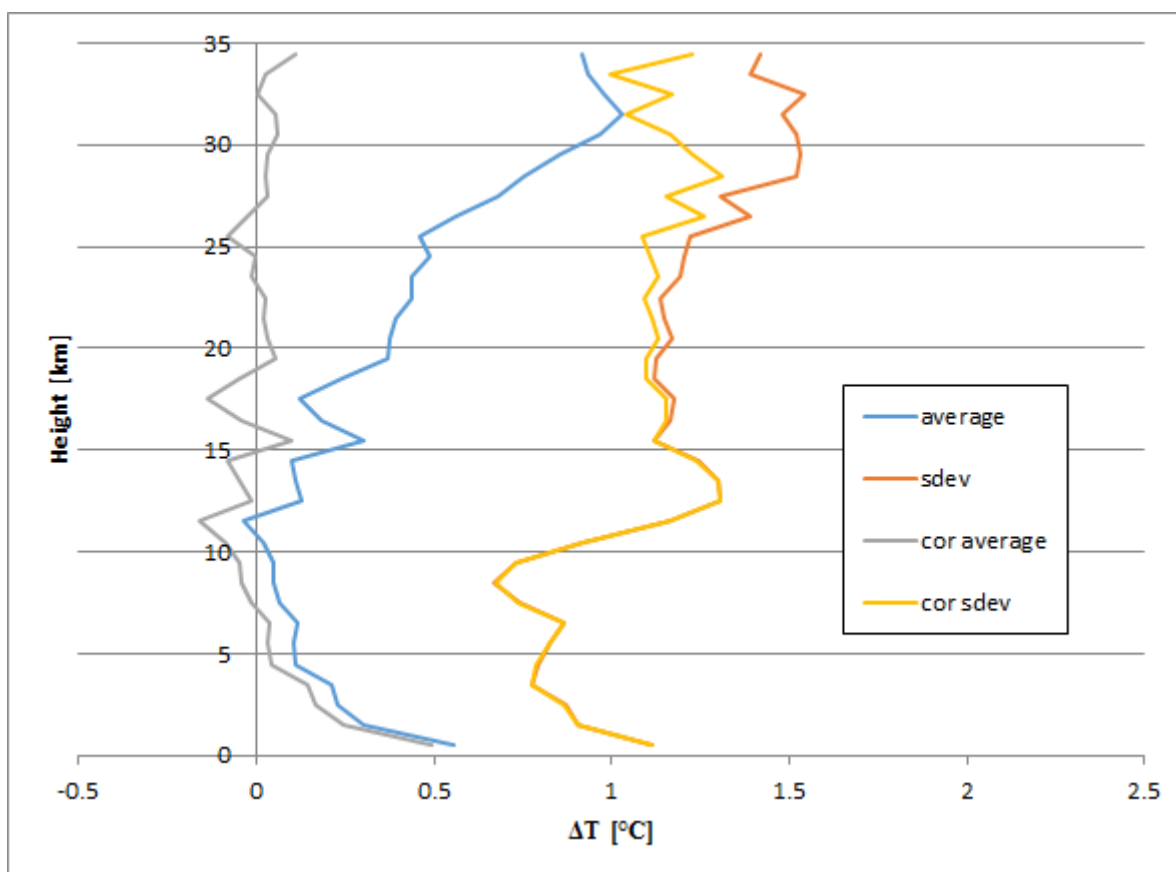
415
 416
 417



418

419 Figure 22 shows the mean and SD of ΔT as a function of height before and after applying the correction. We can see that bias
 420 was almost completely removed, except for the lowest layers, where the bias is expected due to diurnal effects. Another notable
 421 result was that ΔT SD for heights above 20 km was significantly lowered.

422



423

424 Figure 22. Average ΔT and its standard deviation before and after friction correction (Praha-Libus).

425

426 Investigations were extended to other stations to examine consistency. Information about type of the data, data sample and
 427 calculated coefficient are in Table 4.

428

Station	Praha-Libus	Lindenberg	Sola
Country	Czechia	Germany	Norway
Radiosonde	RS41-SG	RS41-SGP	RS41-SGP
Parachute	no	yes	no
Sample start	Jul 2019	Nov 2019	Dec 2019



Sample end	Jan 2020	Feb 2020	Jan 2020
Soundings	554	329	45
Compared levels	527 779	650 399	37 670
Coefficient A	$4.05 \cdot 10^{-4}$	$4.46 \cdot 10^{-4}$	$3.44 \cdot 10^{-4}$

Table 4: Coefficient A determined from different samples

It can be seen from the results in Table 4 that the exact value of the correction coefficient is slightly uncertain. As there is a lot of noise in the data due to other reasons of ΔT than just friction, we would need a larger sample of data to investigate further.

4.2 Indirect effect of heating

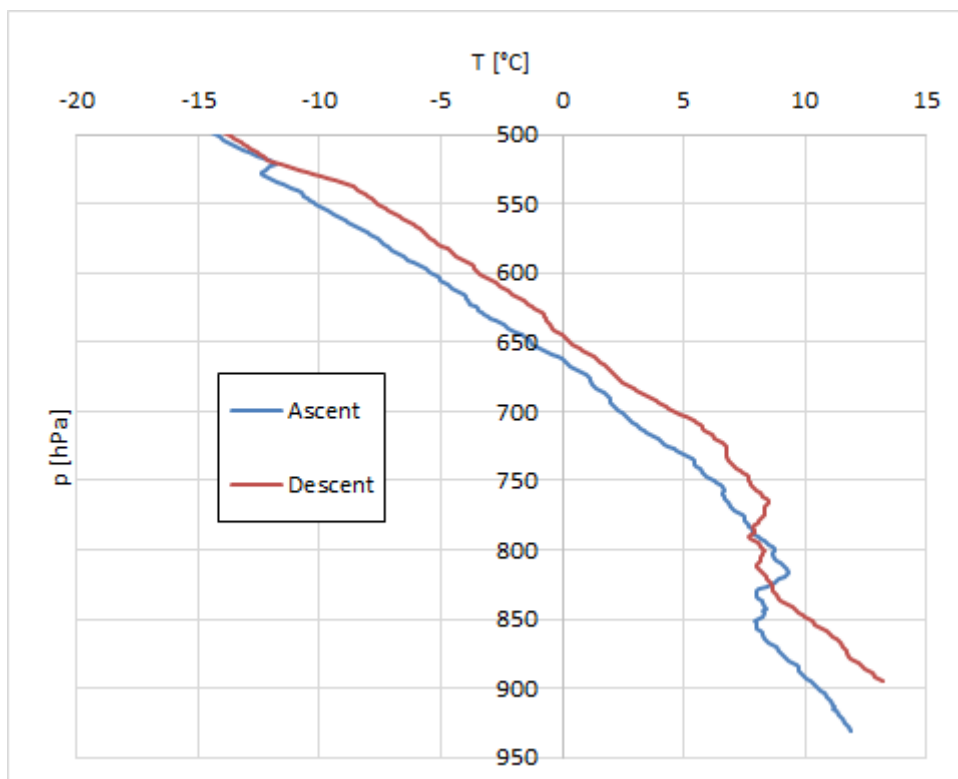
Some radiosondes measure atmospheric pressure using a sensor and the geopotential height is calculated using hydrostatic equilibrium: $dP = -\rho(H) g dH$, where density of air ρ depends on pressure, temperature and humidity of the air. This method is used for processing of the data from RS41-SGP radiosondes. The RS41-SG type of radiosonde measures height using GPS, and the pressure is calculated with the very same equation.

As discussed in the last subsection, during the descent the radiosonde overestimates air temperature, mostly in the stratosphere, where the descent speeds are high enough to have an impact. This overestimation of temperature leads to underestimation of air density. For the RS41-SGP it means that (negative) height increments are smaller than they should be and thus for the certain pressure level, higher altitudes are reported than they should be. As the height errors accumulate during the descent, the shift of height still remains in the troposphere levels, where direct heating impact is negligible.

For the RS41-SG radiosondes, the effect is very similar, resulting in an underestimation of pressure increments, causing a lower pressure for a given height. And vice versa, lower height for the given pressure. Illustration of this effect can be seen in Figure 23.

The shift of the profile is visible only if we use as a vertical coordinate the variable which is calculated, not directly measured. As most applications (including many NWP systems) use pressure as vertical coordinate, the effect can be seen for RS41-SG radiosondes. It should lead to an increase in SD when comparing variables to the NWP model, but also to increase of tropospheric temperature bias due to the temperature gradient in the troposphere (as can be seen in Finnish data compared to ECMWF in Figure 14).

The effect is clearly visible in Figure 24. For the Praha-Libus data sample ascent and descent levels were matched both using height (blue for bias, red for SD) and using pressure (grey for bias, yellow for SD). In the stratosphere the direct heating of the sensor has a major effect on T differences and the lines are almost the same. In the troposphere, the friction is much lower due to the slower DR and for pressure-matched levels, the shift of the profile caused by accumulated pressure errors is responsible for the majority of bias (difference between gray and blue line). Up to 11 km there is also visible worsening of SD for pressure-matched profiles due to this effect.

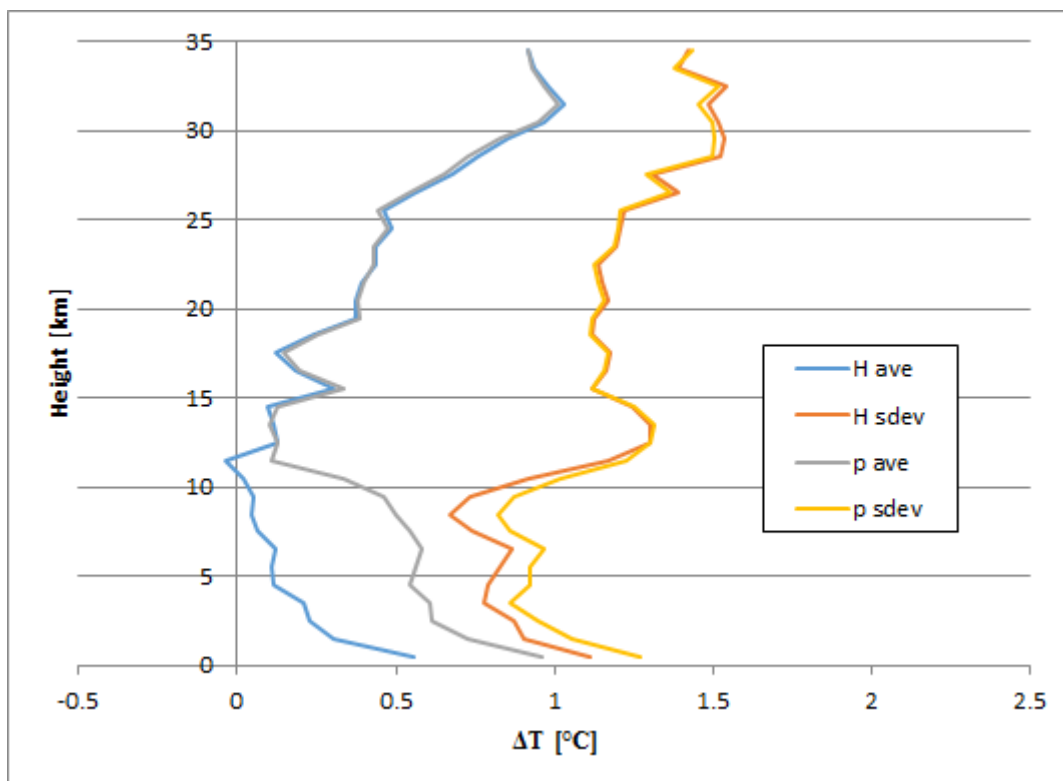


458

459 Figure 23: Shift of the tropospheric profile as a function of pressure. Profile from 23-09-2019, 12 UTC, Praha-Libus.

460

461



462

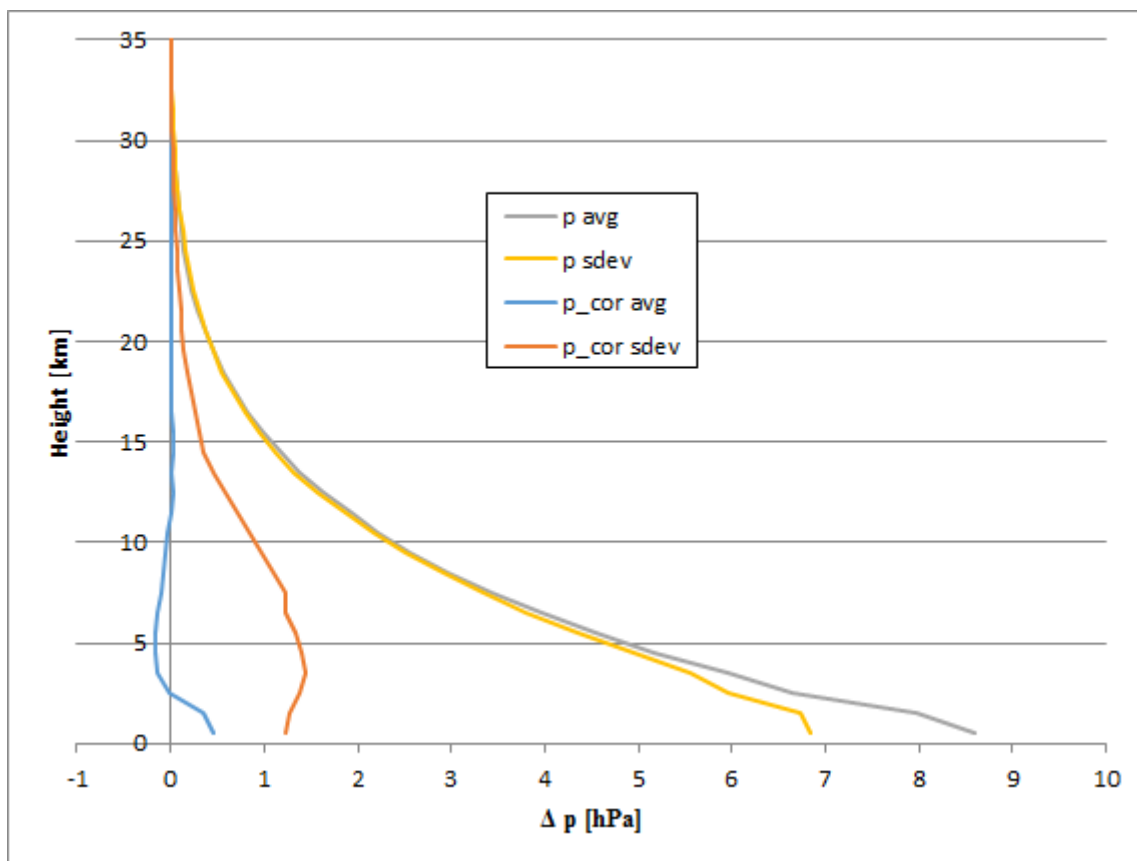
463 Figure 24: T bias and SD when ascent/descent matched used height (blue, red) or matched using pressure (grey, yellow)

464

465 The improvement of pressure differences after application of the temperature correction, Eq (2), and recalculating pressure
466 using corrected temperature is clearly visible in Figure 25. The recalculation was made on a data sample from Praha-Libus,
467 and the pressure bias near the surface was decreased by approximately 95 %.

468

469

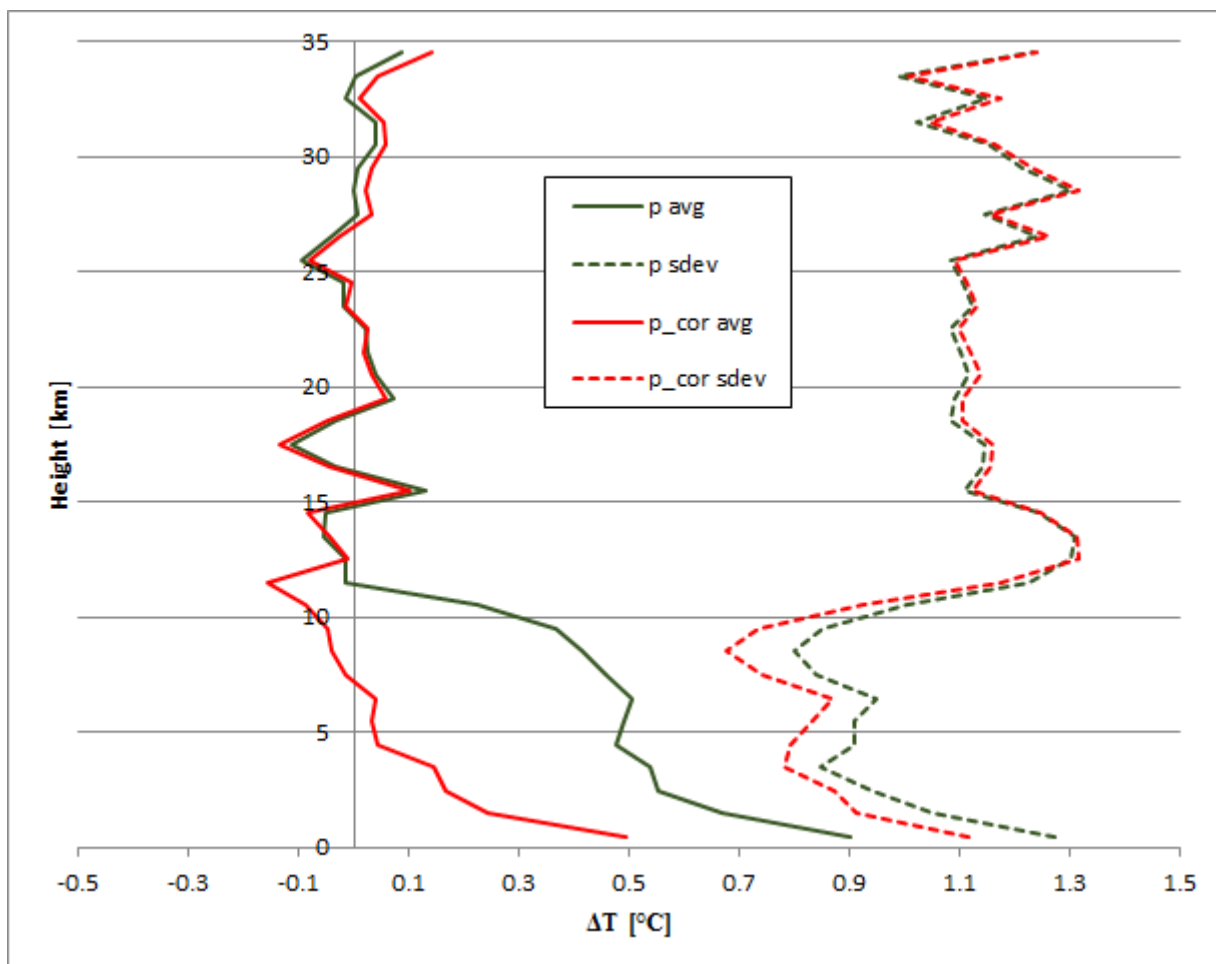


470

471 Figure 25: Average Δp and its standard deviation before and after applying temperature correction for friction and pressure
472 recalculation. For representation purposes is $\Delta p = p_A - p_D$ on this plot.

473

474 The positive effect of the pressure correction was checked using Praha-Libus temperature data. Figure 26 shows the bias (solid)
475 and SD (dashed) relative to the ascent for the two versions of temperature descent data (all the data used T_{cor} according to Eq.
476 (2)). Green lines are for the data matched by reported pressure and red for the data matched by pressure recalculated using
477 corrected temperature. The negative effect of accumulated pressure error due to friction was removed by the pressure
478 correction. The red lines on figure 26 are almost identical with blue and red lines on figure 22 using data matched by height.
479 Overall, it appears that the pressure errors arising from stratospheric heating of the temperature sensor can largely be removed
480 by using corrected temperatures in the hydrostatic calculations.



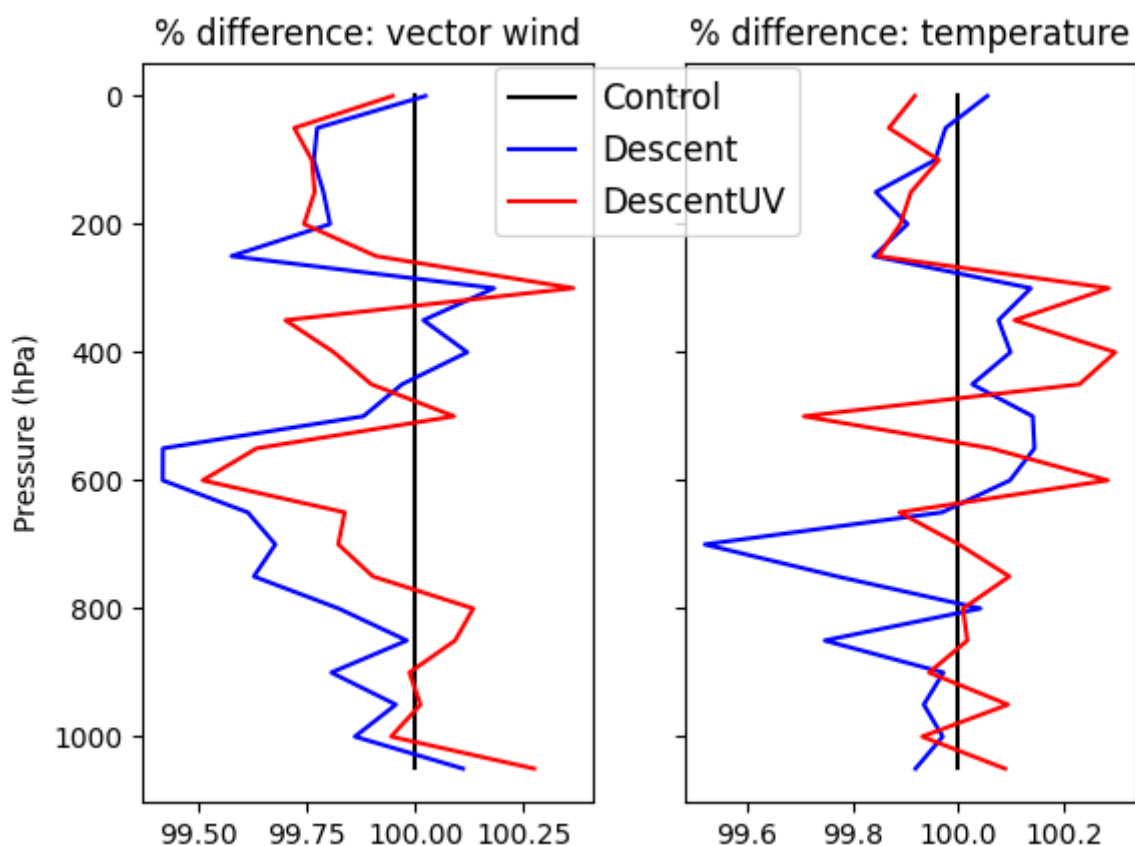
481
482 Figure 26: Temperature bias and SD when as vertical coordinate was used pressure (green) and corrected pressure (red). On
483 all temperatures friction correction was applied.

484 5 Assimilation of descent data

485 Partly prompted by the drop in numbers of aircraft data due to the Covid-19 pandemic (Ingleby et al, 2021) a trial was run
486 assimilating European RS41 descent data for 20 January to 28 April 2020. The large-scale impact was very small as expected,
487 but over Europe there were modest improvements in the fit of the 12 h forecast to radiosonde ascent data (Figure 27). There
488 were improvements over Germany (not shown) and the impact was mixed over Scandinavia. The decision was taken to
489 assimilate only the German descent data for the time being - this is the best subset, because they have parachutes and pressure
490 sensors, as discussed in section 3 - implemented operationally on 17 June 2020. In the final configuration data from 150 hPa
491 down to the surface were used. Upper-level temperatures were excluded because of the biases. Upper-level winds were used
492 in the trial, but there are some concerns about the pressures being less accurate when the radiosonde is falling fast. The use of



493 upper-level descent winds may be reviewed in the future. Note that at the upper-levels the ascent and descent are close together
494 in space and time and so one may not want to assimilate both ascent and descent profiles. As discussed in section 4, some of
495 the bias problems would be reduced if height was used as the vertical coordinate rather than pressure - however this would
496 involve significant work and testing, so there are no plans to do so in the near future.



497
498 Figure 27. Effect of assimilation of all descent data (wind, temperature, humidity; blue line) or just descent winds (red line)
499 2020-01-20 to 2020-04-20. Results are shown for temperature and vector wind fit of 12 hour forecasts to European radiosonde
500 ascents, normalised by the fit of the control forecasts (so values less than 100% indicate improved forecasts).

501 6 Discussion and conclusions

502 The most obvious difference between ascent and descent data is that the descent temperatures are higher at upper levels. This
503 had been noted before for different radiosonde types, by Tiefenau and Gebbeken (1989) and Vencat Ratnam et al. (2014). The
504 latter did not discuss the cause but Tiefenau and Gebbeken (1989) took the descent temperatures as accurate and suggested



505 that the ascent temperatures were too low due to sampling the balloon wake and adiabatic cooling of the gas within the balloon.
506 Whilst wake effects cannot be completely discounted, our results suggest that the descent temperatures are too high and that
507 this is closely linked to the descent rate (Figure 16). In Figure 21 the dependence on descent rate appears quadratic. Vaisala
508 are working on updated processing to address the temperature bias and other issues. There has been considerable discussion
509 on the source of the ascent/descent temperature differences. Whilst we cannot definitively explain the heating mechanism a
510 plausible hypothesis is a conversion of kinetic energy via frictional heating. Clearly the falling radiosonde (plus balloon
511 remains and parachute if fitted) are slowed by friction otherwise it would accelerate to much higher speeds during the descent.
512 Future work might include testing radiosonde sensors in a wind tunnel with a flow of 20 m/s or more to see if the heating is
513 replicated (care would be needed with the reference temperature). We have not been able to find such tests in the literature.
514 There is a paper by de Podesta et al. (2018) about the effect of sensor diameter on temperature errors but they were looking at
515 lower flow rates.

516
517 Another difference, that doesn't seem to have been reported before, is that on average the descent winds are smoother than the
518 ascent winds. In part this seems to reflect the fact that ascents are generally more affected by pendulum motion, however
519 inertial effects and the filtering applied to 'remove' pendulum motion also play a role. The smoother descent winds have a
520 closer RMS fit to the NWP winds, but we cannot currently say whether the ascent or descent winds are more accurate. Most
521 studies of radiosondes concentrate on the temperatures and humidities and the winds are somewhat neglected; the use of long
522 strings improves stratospheric temperatures at the expense of increasing the pendulum motions. For aircraft the winds have
523 more than twice the impact of the temperatures on the quality of short-range forecasts (Ingleby et al, 2021) and forecast
524 sensitivity diagnostics suggest that the same is true of radiosondes (Pauley and Ingleby, 2021), partly because satellite
525 instruments primarily provide temperature and humidity data. Experience shows that GPS winds are generally good quality
526 and biases do not seem to be a problem. GPS can provide high vertical resolution winds - but this makes pendulum motion
527 more obvious and avoidance or removal of pendulum motion deserves more attention. Sako and Walterscheid (2016) discuss
528 empirical filtering of wind profiles from radiosondes and Jimsphere balloons used specifically for wind measurement. It seems
529 likely that dropsonde wind profiles are closer to the true winds (Wang et al, 2008) than radiosonde ascent or descent winds.
530 The two balloon ascents of Kräuchi et al. (2016) largely eliminate pendulum motion but need more evaluation.

531
532 Some aspects of the descent data can be improved by estimating and removing heating effects due to high fall rates (on the
533 temperature, and also on the pressure for radiosondes without a pressure sensor). The descent characteristics are more variable
534 than ascent rates in that for balloons with parachutes, the manner in which the parachute deploys can affect the amplitude of
535 the pendulum motion and the descent speed. It is also likely that there can be improvements in the filtering of pendulum
536 motion. Vaisala are working on these aspects but are not yet ready to give a timescale for changes. In principle users could
537 apply bias corrections, but improving the winds is difficult if they have already been filtered. On the whole, it is simplest to
538 stick to the current practice of manufacturers providing best estimate profiles, but more details of the processing would be



539 welcome and this area should be kept under review. On a similar note there is a question of whether there should be a GRUAN
540 descent product for the RS41 - more work on the uncertainties would be needed for this. There is the wider question of how
541 much the lessons learnt from the RS41 descent are applicable to other radiosondes such as the Meteomodem M10. There is
542 some evidence that pressure sensor accuracy is worse whilst falling fast, but more work on this is needed. However the fall
543 speed should have very little effect on the accuracy of GPS derived positions, because the GPS satellites are moving much
544 faster anyway.

545
546 There is evidence that use of parachutes and/or pressure sensors gives some improvement to the descent data (this will reduce
547 with improved processing/bias correction). There is also the possibility of installing extra receivers so as to obtain more descent
548 data from the lower troposphere (this has been demonstrated in Corsica, Peyrat, pers. comm. 2020). Whether the extra costs
549 are worthwhile would need to be assessed. We note that the impact of extra radiosonde profiles over well-observed Europe
550 will be less than the impact of extra profiles near remote islands or ships. In May 2021 descent data was received from several
551 European ships in the North Atlantic and also a station in Antarctica. ECMWF and DWD have started operational assimilation
552 of a subset of descent profiles - excluding the stratospheric segment with higher average fall rates (arguably it would be better
553 to exclude data based on the actual descent rate, but this is not reported, it is also desirable to exclude values where there are
554 particularly large accelerations, e.g. Fig. 5). The US Navy global model is assimilating all available descent profiles (Pauley,
555 pers. comm. 2021), we are not aware of other NWP systems using them yet. NWP systems generally use pressure as the vertical
556 coordinate for radiosonde data, arguably there would be advantages in using height instead. There has been much more use of
557 NWP model fields in this investigation than is traditional for development/validation of in situ observations (but routine now
558 for new satellites - Newman et al. 2020). This means that a much larger sample can be examined. Note that traditional
559 radiosonde intercomparisons (e.g., Nash et al, 2011) can't be used to assess descent data because the multi-radiosonde rig used
560 has various implications for the descent including possible entanglement.

561 **7 Appendix: comparison with aircraft temperatures**

562 For cruise level aircraft (typical speed is about 250 m/s) the measured temperature, known as total air temperature (TAT), can
563 be more than 20 K higher than the static air temperature (SAT). The link between TAT and SAT (Wendisch and Brenguier,
564 2013) can be expressed with equation:

$$565 \quad SAT = \frac{TAT}{1 + \frac{r(\gamma-1)}{2} M^2} \quad [A1],$$

566 where r is the recovery factor of the sensor, γ adiabatic index and M is Mach number.

567 From equation [A1] we can get the difference $TAT - SAT = SAT \cdot \frac{r(\gamma-1)}{2} \cdot M^2$

568 If we use the Mach number: $M = \frac{v}{a}$,



569 where v is the airspeed of the object (aircraft or radiosonde) and a the speed of sound, given by: $a = \sqrt{\gamma \cdot (C_p - C_v) \cdot SAT}$,

570 where C_p and C_v are heat capacity constants for constant pressure and volume respectively,

571 we can get: $TAT - SAT = \frac{r(\gamma-1)}{2} \cdot \frac{v^2}{\gamma \cdot (C_p - C_v)}$ [A2]

572 Applying $\gamma = \frac{C_p}{C_v}$ to equation [A2], the difference between measured and real temperature is:

573 $TAT - SAT = \frac{v^2}{2C_p} r$ [A3],

574 According to the Wikipedia entry on Total air temperature, the typical recovery factor for platinum wire (which is used for
575 radiosondes) is 0.75 – 0.9. Even if we are not sure about the exact physical process of kinetic energy transfer to internal heat
576 in case of radiosondes, we might expect similar behavior (quadratic dependency on descent rate, but independent of height,
577 temperature and air density). When we apply the equation A3 to descending radiosondes, where v is the descent rate (DR) of
578 the radiosonde, with the range 0.75 - 0.9 for r we get:

579 $TAT - SAT = A \cdot 10^{-4} \cdot DR^2$ with A in the range 3.70 to 4.47. [A4]

580 However, the similar coefficients for aircraft and descent radiosondes may come from different conversion mechanisms..

581

582 **Data availability statement**

583 The radiosonde descent data for September-November 2019 are available in BUFR format from
584 <https://www.gruan.org/data/data-packages/dpkg-2021-2>. Radiosonde ascent data in BUFR format are available from
585 <https://www.ncei.noaa.gov/pub/data/igra/v1/related/BUFR/ecmwf/data/> (see Geller et al, 2021). BUFR decoding tools are
586 available from ecCodes (with examples of radiosonde decoders at https://confluence.ecmwf.int/display/ECC/bufr_read_tempf
587). Other decoders are also available, e.g. <https://github.com/NOAA-EMC/NCEPLIBS-bufr/tree/master>.

588 **Author contributions**

589 BI with help from DE worked on paper conceptualization and on the methodology. BI, MM and GM performed the formal
590 analysis and visualisation. All the co-authors contributed to the writing of the paper, review and editing. Data curation was by
591 MS, BI and DE.

592 **Competing interests**

593 The authors declare that they have no conflict of interest.

594 **Acknowledgements**

595 The authors would like to thank the meteorological services that provided, and continue to provide, descent data. Michael de
596 Podesta (NPL) gave useful advice on the measurement of temperature by a moving sensor. Some early work on descent data



597 was performed by Christopher Wyburn-Powell as a vacation student at the Met Office in summer 2018. Lars Isaksen and Sean
598 Healy of ECMWF made suggestions that improved the manuscript.

599 References

- 600 Bodeker, G. E., Bojinski, S., Cimini, D., Dirksen, R. J., Haeffelin, M., Hannigan, J. W., Hurst, D. F., Leblanc, T., Madonna,
601 F., Maturilli, M., Mikalsen, A. C., Philipona, R., Reale, T., Seidel, D. J., Tan, D. G. H., Thorne, P. W., Vömel, H., and Wang,
602 J. (2016). Reference Upper-Air Observations for Climate: From Concept to Reality, *Bulletin of the American Meteorological*
603 *Society*, 97(1), 123-135. <https://dx.doi.org/10.1175/BAMS-D-14-00072.1>
- 604 de Podesta, M., Bell S., and Underwood R.: Air temperature sensors: dependence of radiative errors on sensor diameter in
605 precision metrology and meteorology. *Metrologia*, 55, 229. 2018
- 606 Dirksen, R. J., Sommer, M., Immler, F. J., Hurst D. F., Kivi R., and Vömel H.: Reference quality upper-air measurements:
607 GRUAN data processing for the Vaisala RS92 radiosonde. *Atmos. Meas. Tech.*, 7, 4463-4490, doi:10.5194/amt-7-4463-2014,
608 2014
- 609 Geller, M. A., Love, P. T., Ingleby, B., Yin, X., 2021: New Availability of High Vertical-Resolution Radiosonde Data for
610 Research New Availability of High Vertical-Resolution Radiosonde Data for Research. SPARC Newsletter, No 56, pp 14-15,
611 2021 <https://www.sparc-climate.org/publications/newsletter/sparc-newsletter-no-56/>
- 612 Harrison, R.G. and Hogan, R.J., 2006. In situ atmospheric turbulence measurement using the terrestrial magnetic field—a
613 compass for a radiosonde. *Journal of Atmospheric and Oceanic Technology*, 23(3), pp.517-523.
- 614 Hock, T. F. and Franklin J. L.: The NCAR GPS Dropwindsonde. *Bull. Amer. Meteor. Soc.*, 80, 407–420,
615 [https://doi.org/10.1175/1520-0477\(1999\)080<0407:TNGD>2.0.CO;2](https://doi.org/10.1175/1520-0477(1999)080<0407:TNGD>2.0.CO;2), 1999
- 616 Hurst, D. H., Oltmans, S. J., Vömel, H., Rosenlof, K. H., Davis, S. M., Ray, E. A., Hall, E. G., and Jordan, A. F.: Stratospheric
617 water vapor trends over Boulder, Colorado: Analysis of the 30 year Boulder record, *J. Geophys. Res.*, 116,
618 D02306, doi:10.1029/2010JD015065, 2011.
- 619 Ingleby, B., 2017: An assessment of different radiosonde types 2015/2016. ECMWF Technical Memorandum 807.
- 620 Ingleby, B., Candy, B., Eyre, J., Haiden, T., Hill, C., Isaksen, L., Kleist, D., Smith, F., Steinle, P., Taylor, S., Tennant, W.,
621 and Tingwell, C.: The impact of COVID-19 on weather forecasts: a balanced view. *Geophys. Res. Lett.* 2021
- 622 Ingleby B., L. Isaksen, T. Kral, T. Haiden, M. Dahoui, 2018: Improved use of atmospheric *in situ* data. ECMWF Newsletter
623 155, pp 20-25 <https://www.ecmwf.int/en/elibrary/18208-improved-use-atmospheric-situ-data>
- 624 Lomb, N.R. Least-squares frequency analysis of unequally spaced data. *Astrophysics and space science*, 39(2):447–462, 1976.
- 625 Luers, J.K. and Eskridge, R.E. Use of radiosonde temperature data in climate studies. *Journal of climate*, 11(5):1002–1019,
626 1998.
- 627 MacCready, P.B., 1965: Comparison of Some Balloon Techniques. *J. Appl. Meteor.*, 4, 504-508, [https://doi.org/10.1175/1520-](https://doi.org/10.1175/1520-0450(1965)004<0504:COBT>2.0.CO;2)
628 [0450\(1965\)004<0504:COBT>2.0.CO;2](https://doi.org/10.1175/1520-0450(1965)004<0504:COBT>2.0.CO;2)



- 629 Madonna, F., Kivi, R., Dupont, J.-C., Ingleby, B., Fujiwara, M., Romanens, G., Hernandez, M., Calbet, X., Rosoldi, M.,
630 Giunta, A., Karppinen, T., Iwabuchi, M., Hoshino, S., von Rohden, C., and Thorne, P. W.: Use of automatic radiosonde
631 launchers to measure temperature and humidity profiles from the GRUAN perspective. *Atmos. Meas. Tech.*, 13, 3621–3649,
632 <https://doi.org/10.5194/amt-13-3621-2020>, 2020.
- 633 Marlton, G.J., Giles Harrison, R., Nicoll, K.A. and Williams, P.D.: Note: A balloon-borne accelerometer technique for
634 measuring atmospheric turbulence. *Review of Scientific Instruments*, 86(1), p.016109. 2015
- 635 Marlton, G.J., 2016. *On the development, characterisation and applications of a balloon-borne atmospheric turbulence sensor*
636 (Doctoral dissertation, University of Reading).
- 637 Nash J., T. Oakley, H. Vömel, and Wei LI.: WMO Intercomparison of High Quality Radiosonde Systems Yangjiang, China,
638 12 July - 3 August 2010, WMO Instruments and Observing Methods Report No. 107. 2011
- 639 Newman, S., Carminati, F., Lawrence, H., (...), Salonen, K., Bell, W.: Assessment of new satellite missions within the
640 framework of numerical weather prediction. *Remote Sensing* 12(10), 1580, 2020
- 641 Pauley P, and Ingleby B.: Assimilation of in-situ observations. In: Park SK, Xu L (eds) *Data Assimilation for Atmospheric,*
642 *Oceanic and Hydrologic Applications (Vol. IV)*. Springer, in print. 2021
- 643 Seidel DJ, Sun B, Pettey M, Reale A. 2011. Global radiosonde balloon drift statistics, *J. Geophys. Res.*, 116 : D07102,
644 doi:10.1029/2010JD014891.
- 645 Shepherd, T. G., I. Polichtchouk, R. J. Hogan and A. J. Simmons, 2018: Report on Stratosphere Task Force. ECMWF Technical
646 Memorandum 824.
- 647 Shimizu, K. and Hasebe, F.: Fast-response high-resolution temperature sonde aimed at contamination-free profile observations,
648 *Atmos. Meas. Tech.*, 3, 1673-1681, <https://doi.org/10.5194/amt-3-1673-2010>, 2010.
- 649 Tiefenau, H. K. E. and Gebbeken, A.: Influence of meteorological balloons on temperature measurements with radiosondes:
650 night-time cooling and daytime heating. *J. Atmos. Ocean. Tech.*, 6, 36-42, 1989.
- 651 Kräuchi A., R. Philipona, G. Romanens, D. F. Hurst, E. G. Hall, and A. F. Jordan, 2016: Controlled weather balloon ascents
652 and descents for atmospheric research and climate monitoring. *Atmos. Meas. Tech.*, 9, 929-938, doi:10.5194/amt-9-929-2016
- 653 Vaisala, 2017, Vaisala RS41SG datasheet, *Vaisala* [https://www.vaisala.com/sites/default/files/documents/WEA-MET-RS41-](https://www.vaisala.com/sites/default/files/documents/WEA-MET-RS41-Datasheet-B211321EN.pdf)
654 [Datasheet-B211321EN.pdf](https://www.vaisala.com/sites/default/files/documents/WEA-MET-RS41-Datasheet-B211321EN.pdf)
- 655 Venkat Ratnam, M., Pravallika, N., Ravindra Babu, S., Basha, G., Pramitha, M., and Krishna Murthy, B. V., 2014: Assessment
656 of GPS radiosonde descent data, *Atmos. Meas. Tech.*, 7, 1011-1025
- 657 Söder, J., Gerding, M., Schneider, A., Dörnbrack, A., Wilms, H., Wagner, J., and Lübken, F.-J.: Evaluation of wake influence
658 on high-resolution balloon-sonde measurements, *Atmos. Meas. Tech.*, 12, 4191–4210, [https://doi.org/10.5194/amt-12-4191-](https://doi.org/10.5194/amt-12-4191-2019)
659 [2019](https://doi.org/10.5194/amt-12-4191-2019), 2019.
- 660 Wagner N.K., 1964: Theoretical accuracy of a meteorological rocketsonde thermistor. *J Appl. Meteor*, 3, 461-469
- 661 Wang, J., Bian, J., Brown, W. O., Cole, H., Grubisic, V., and Young, K.: Vertical air motion from T-REX radiosonde and
662 dropsonde data, *J. Atmos. Ocean. Tech.*, 26, 928-942, 2008.



663 Wendisch, M., Brenguier, J.-L.: Airborne Measurements for Environmental Research: Methods and Instruments, Wiley,
664 641pp.

665 WMO, 2018a: Guide to Instruments and Methods of Observation, Vol I—Measurement of meteorological variables. WMO-
666 No. 8, 548pp, https://library.wmo.int/doc_num.php?explnum_id=10179

667 WMO, 2018b: Guide to Instruments and Methods of Observation, Vol III—Observing Systems. WMO-No. 8, 426pp,
668 https://library.wmo.int/doc_num.php?explnum_id=9872

669 WMO, 2019: Manual on Codes, Vol. I.2, Part B—Binary Codes and Part C—Common Features to Binary and Alphanumeric
670 Codes. WMO-No. 306, 1180 pp, https://library.wmo.int/doc_num.php?explnum_id=10310.

671 World Meteorological Organization, 1994: The difference in observed temperatures from radiosondes suspended 10 m and 40
672 m beneath a 1400 g balloon (J.B. Elms, J. Nash and G. Williams). Papers Presented at the WMO Technical Conference on
673 Instruments and Methods of Observation (TECO-94), Instruments and Observing Methods Report No. 57,
674 WMO/TD-No. 588, Geneva, pp. 121-126. https://library.wmo.int/pmb_ged/wmo-td_588.pdf

675 Zhang J, Chen H, Zhu Y, Shi H, Zheng Y, Xia X, Teng Y, Wang F, Han X, Li J, Xuan Y. A Novel Method for Estimating the
676 Vertical Velocity of Air with a Descending Radiosonde System. *Remote Sensing*. 2019; 11(13):1538.
677 <https://doi.org/10.3390/rs11131538>

678